Assessing a Satellite-Era Perspective of the Global Water Cycle

C. ADAM SCHLOSSER

Joint Program on the Policy and Science of Global Change, Massachusetts Institute of Technology, Cambridge, Massachusetts

PAUL R. HOUSER

Climate Dynamics Program, Center for Research on Environment and Water, George Mason University, Fairfax, Virginia

ABSTRACT

The capability of a global data compilation, largely satellite based, is assessed to depict the global atmospheric water cycle's mean state and variability. Monthly global precipitation estimates from the Global Precipitation Climatology Project (GPCP) and the Climate Prediction Center (CPC) Merged Analysis of Precipitation (CMAP) span from 1979 to 1999. Monthly global Special Sensor Microwave Imager (SSM/I)-based bulk aerodynamic ocean evaporation estimates span from June 1987 to December 1999. Global terrestrial evapotranspiration rates are estimated over a multidecade period (1975–99) using a global land model simulation forced by bias-corrected reanalysis data. Monthly total precipitable water (TPW) from the NASA Global Water Vapor Project (NVAP) spans from 1988 to 1999.

The averaged annual global precipitation (P) and evaporation (E) estimates are out of balance by 5% or 24 000 (metric) gigatons (Gton) of water, which exceeds the uncertainty of global mean annual precipitation ($\sim\pm1\%$). For any given year, the annual flux imbalance can be on the order of 10% (48 000 Gton of water). However, observed global TPW interannual variations suggest a water flux imbalance on the order of 0.01% (48 Gton of water)—a finding consistent with a general circulation model (GCM) simulation. Variations in observationally based global P and E rates show weak monthly and interannual consistency, and depending on the choice of ocean evaporation data, the mean annual cycle of global $E - P$ can be up to 5 times larger to that of TPW. The global ocean annual evaporation rates have as much as a $\sim1\%$ yr^{-1} increase during the period analyzed (1988–99), which is consistent in sign with most transient CO_2 GCM simulations, but at least an order of magnitude larger. The ocean evaporation trends are driven by trends in SSM/I-retrieved near-surface atmospheric humidity and wind speed, and the largest year-to-year changes are coincident with transitions in the SSM/I fleet.

In light of (potential) global water cycle changes in GCM projections, the ability to consistently detect or verify these changes in nature rests upon one or more of the following: quantification of global evaporation uncertainty, at least a twofold improvement in consistency between the observationally based global precipitation and evaporation variations, a two order of magnitude rectification between annual variations of $E - P$ and precipitable water as well as substantial improvements in the consistency of their seasonal cycles, a critical reevaluation of intersatellite calibration for the relevant geophysical quantities used for ocean evaporation estimates, and the continuation of a dedicated calibration in this regard for future satellite transitions.

1. Introduction

Among the most compelling global climate change manifestations would be an intensification of the global water cycle, characterized by increased global precipitation, evaporation, river discharge, and exacerbations of extreme hydrologic regimes, such as floods and droughts. The underpinning question is to what extent global climate change (anthropogenic or natural) entails an associated water cycle response, which is fundamentally a manifestation of changes in event-based characteristics (i.e., storms and dry periods) and process-level biogeophysics (i.e., evapotranspiration). To date, many studies have diagnosed the existence and tested the significance of secular trends in particular hydrologic variables and events over a wide range of spatiotemporal scales (e.g., Groisman et al. 2004, 2005; Roy and Balling 2004; New et al. 2001; Diaz et al. 2001; Verschuren et al. 2000; Wentz and Schabel 2000; Lettenmaier et al. 1994). In addition, the sensitivity of

Corresponding author address: C. Adam Schlosser, MIT, E40-413, 1 Amherst St., Cambridge, MA 02048.
E-mail: casch@mit.edu

hydrologic states and fluxes to climate variations (e.g., Soden 2000; Curtis et al. 2001; Mischwaner and Dessler 2004), as well as implications of the observational uncertainty in global hydrologic simulations (e.g., Fekete et al. 2004), have been examined. In other studies, observed and modeled trend and variability diagnostics have been compared (e.g., Bosilovich et al. 2005; Kiktev et al. 2003; Soden 2000) and hydrologic products from model reanalyses assessed (e.g., Trenberth and Guillemot 1998; Roads et al. 1999). Finally, investigations with climate models have provided insights as to plausible changes that can be expected in the global water cycle under anthropogenically forced climate change (e.g., Yang et al. 2003; Räisänen 2002; Milly et al. 2002; Allen and Ingram 2002). Underpinning all these studies is an unambiguous requirement for climate-quality, globally complete observations of the key water cycle rates (i.e., precipitation and evaporation) and storages (e.g., water vapor). Regardless of the extent to which multiple sources of data (i.e., in situ or remotely sensed) will be used to construct these fields, it is reasonable to expect satellite-based measurements to provide a substantial portion of the information, particularly in areas where on-site measurements are sparse or impractical. However, a key issue that remains is an assessment of the degree to which our satellite-based observational capabilities provide a balanced, consistent global water cycle depiction. A wealth of satellite data, data assimilation, and model capabilities has been developed over the past few decades in support of this goal. Furthermore, a call for this type of analysis has also been suggested more than a decade ago (e.g., Kinter and Shukla 1990), in addition to more recent charges by the scientific community (e.g., Hornberger et al. 2001; Houser and Entin 2005).

The purpose of this study, therefore, is to assess the capability of a global data compilation, largely satellite based, to faithfully depict global water fluxes, and the extent to which their spatiotemporal variations are consistent to each other and to complementary water storage variations. The analysis will also explore the existence of large *global-scale* signals and/or trends in the data and ascertain their causes. In the next section, the observationally based data and model calculations used for this study are described. Data analyses are given in section 3, and concluding remarks and future observational challenges and prospects are given in section 4.

2. Data

a. Global water budget synthesis inputs

Data were collected for this study deliberately from disparate satellite-based sources with the intent to con-struct global water cycle budgets and rates, keeping in mind that most blended global data products combine different information over land than over ocean regions. As such, this analysis focuses on six core datasets:

- the Global Precipitation Climatology Project (GPCP) version 2,
- the Climate Prediction Center (CPC) Merged Analysis of Precipitation (CMAP),
- Goddard Satellite-based Surface Turbulent Fluxes version 2 (GSSTF),
- Hamburg Ocean Atmosphere Parameters and Fluxes from Satellite data (HOAPS),
- Center for Ocean–Land–Atmosphere Studies (COLA) Global Offline Land surface Datasets (GOLD), and
- National Aeronautics and Space Administration (NASA) Global Water Vapor Project (NVAP).

Recently, Mehta et al. (2005) evaluated a subset of the above-mentioned observationally based datasets, and found that the degree of consistency in the resulting annual cycle of cross-equatorial freshwater transport is dependent to the choice of the global precipitation datasets analyzed. Furthermore, their analyses underscored the important role the oceans play in the global freshwater budget. Their analysis focused primarily on the annual cycle of the global water budget collection, and emphasize that a more quantitative evaluation was not possible due to a lack of error estimates in the global precipitation (P), evaporation (E), and their differences ($E - P$). Here, we address some of these shortcomings by considering a larger selection of observationally based datasets, and focus on the interannual variations, trends (if any), and balances of the key quantities—judged against quantitative global precipitation error estimates. To supplement this analysis in terms of a "baseline of consistency" among the disparate global water flux observational estimates, global water fluxes from a multidecadal simulation produced by an atmospheric general circulation model (AGCM) are also considered. A brief description of each dataset follows here, with references pointing to more detailed documentation.

The GPCP version 2 monthly precipitation dataset (Adler et al. 2003) is a globally complete precipitation analysis that is produced by blending low-orbit microwave and geosynchronous infrared satellite retrievals with surface gauge observations. The data are projected on a $2.5° \times 2.5°$ grid and span the years 1979 to the present. However, the microwave satellite retrievals were available only from 1987 to the present. Monthly merged precipitation random error estimates have also been constructed based on the techniques of Huffman

(1997). Many other satellite-based, in situ, and blended global precipitation estimates exist, and have been successful at identifying key regional patterns of precipitation anomalies associated with major modes of climate variability, such as El Niño–Southern Oscillation (ENSO; e.g., Kidd 2001 and New et al. 2001 provide nice summaries). Although a recent precipitation–algorithm comparison effort (Adler et al. 2001) indicates the range of global-scale precipitation estimates (considering all satellite, in situ, model-based, and climatological products available) is as large as a factor of 2–3, the merged data products (such as GPCP and CMAP) provide the overall "best" results. CMAP (Xie and Arkin 1997) is another global precipitation product that serves to combine all relevant satellite and in situ data. Yin et al. (2004) describe key distinctions between GPCP and CMAP. Among the more notable differences is the use of atoll data. GPCP chooses not to use these data, and as such, there is a 16% bias when judged over these regions. On the use of atoll data, Adler et al. (2003) states, "it is possible that the satellite technique is underestimating the precipitation, but there is also the possibility that the atoll gauges are not completely representative of open-ocean precipitation. Because of this question and the fact that the atoll stations are only located in the western Pacific Ocean and are, therefore, not representative of the entire tropical ocean, the GPCP dataset has not been adjusted . . . " The results of Yin et al. (2004) support this decision by finding that the GPCP data are more accurate in their over-ocean diagnostics. Nevertheless, the debate on the representativeness of the atoll data will continue. Notwithstanding issues regarding data-source selection, both datasets have significant deficiencies in resolving orographic effects (e.g., Basist et al. 1994; Nijssen et al. 2001). This poses a challenge for the various global collection efforts to ultimately augment. However, agency-level efforts involving coordinated, multiple investigations are under way to do so (e.g., Houser and Entin 2005), and thus more accurate and comprehensive global precipitation data, in this regard, are foreseeable.

The GSSTF dataset (Chou et al. 2003) contains gridded fields at $1° \times 1°$ resolution of daily, monthly, and annual bulk aerodynamic estimates of global ocean heat fluxes. HOAPS (Fairall et al. 1996; Bentamy et al. 2003; data available through the World Data Center for Climate, Hamburg, Germany, see online at http://cera-www.dkrz.de/CERA/) is quite similar in its construction to the GSSTF data. For both ocean datasets, satellite-based data [e.g., from the Special Sensor Microwave Imager (SSM/I)] are used to derive an ocean latent heat flux estimate based on the bulk aerody-

namic formulation (no-slip conditions at the surface) given by

$$LH = \rho L_v C_E |V|(Q_s - Q_a), \qquad (1)$$

where LH is the latent heat flux (W m^{-2}), ρ is the density of air, C_E is the bulk transfer coefficient at the reference height, $|V|$ is the wind speed at a reference height (=10 m), Q_a is the specific humidity at the reference height, Q_s is the saturation specific humidity that is a function of sea surface temperature (SST), and $(Q_s - Q_a)$ is the sea–air humidity difference. The value of C_E is adjusted according to stability and salinity (for GSSTF only) conditions. Furthermore, GSSTF uses SSM/I version 4 wind speed products (Meissner et al. 2001); on the other hand, HOAPS uses the Goodberlet algorithm (Bentamy et al. 1999) with SSM/I brightness temperature data. For Q_a, GSSTF employs a second-order EOF expansion to fit a humidity profile with (version 4) SSM/I precipitable water retrievals, while HOAPS2 uses an improved Schulz inverse model (Bentamy et al. 2003) with SSM/I brightness temperatures. To convert these latent heat flux estimates to water flux units, we apply the following relation:

$$E_o = L_v^{-1}LH, \qquad (2)$$

where E_o is the ocean evaporation rate, and L_v is the latent heat of vaporization (in this study, assumed constant at its 20°C value = 2.45×10^6 J kg^{-1}). Deviations about its assumed constant value (at 20°C) vary by $\pm 2\%$ corresponding to a $\mp 20°$C change. However, when considering the high correlation between temperature and latent heat flux over oceans (i.e., generally speaking, warmer ocean regions will have higher latent heat fluxes), the resulting biases (using the constant value of L_v above) between warm and cold ocean regions largely offset. So the overall effect on the *global* ocean estimate is likely less than 1%. Other ocean evaporation estimates exist based on bulk aerodynamic methods (this study using the GSSTF and HOAPS data), which have outstanding issues (e.g., Curry et al. 2004). However, most comparison studies to date, using limited evaluation data (e.g., Kubota et al. 2003), indicate that the GSSTF algorithm is not biased compared to other bulk estimates (e.g., Brunke et al. 2003; Curry et al. 2004). Moreover, the GSSTF dataset has skillfully identified key regional variabilities of ocean evaporation, such as those tied to westerly wind bursts as observed by the Tropical Ocean Global Atmosphere Coupled Ocean–Atmosphere Response Experiment (TOGA COARE) fluxes (e.g., Chou et al. 2000).

GOLD is a global, spatially, and temporally continuous land surface dataset that spans 1979–99 (Dirmeyer and Tan 2001). A land surface scheme (LSS) is run at a

T63 equivalent grid box resolution (1.875° × ~1.875°) without feedback to an atmospheric circulation model, creating a self-consistent, global, land surface state time series. The meteorological reanalysis required to temporally integrate the model was obtained from the National Centers for Environmental Prediction–National Center for Atmospheric Research (NCEP–NCAR) reanalysis, and the precipitation was further bias corrected according to the monthly CMAP climatology. The product used for this study is in the form of monthly mean grids over all ice-free land points. Recently, Dirmeyer et al. (2004) has demonstrated that GOLD performs consistently well, and in most cases superior, to other long-term land surface model, coupled land–atmosphere reanalyses soil-wetness products, and satellite-derived estimates. Furthermore, an updated version of the simulation—GOLD2 (P. A. Dirmeyer 2005, personal communication) has been recently provided for evaluation. The GOLD2 simulation differs from its predecessor in that it represents simulations from an upgraded version of the COLA Simplified. Simple. Biosphere (SSiB) land model, driven by the 40-yr European Centre for Medium-Range Weather Forecasts (ECMWF) Re-Analysis (ERA-40; e.g., Hollingsworth and Pfrang 2005) data with the precipitation scaled to agree with the Climate Research Unit (CRU) precipitation on the monthly mean time scale. The entire simulation spans the years 1959–2002, with the years 1957–58 used for spinup. Thus, the GOLD2 simulation may be used similarly as in GOLD for the global budget synthesis. Nevertheless, the GOLD evapotranspiration products are model-based estimates. While the capability to produce satellite-based land evaporation estimates has seen considerable strides recently (e.g., Diak et al. 2004), this particular study requires a long-term estimate of global water fluxes that sufficiently overlaps the ocean and atmospheric data, which at present is unavailable using satellite-based techniques. The GOLD datasets are among many model-based land evaporation estimates (e.g., Rodell et al. 2004) that have recently emerged. However, in the context of gauging the range of land model estimates (with potentially some measure of "uncertainty"), the current Global Energy and Water Cycle Experiment (GEWEX) Global Soil Wetness Project Phase 2 (GSWP2; Dirmeyer et al. 2002) provides global simulations of continental evaporation, as estimated by as many as 13 different land models, for the years 1986–95 (a shorter time period than that considered in this study) forced with the International Satellite Land Surface Climatology Project, Initiative II (ISLSCP II) atmospheric variables and soil–vegetation parameters.

Preliminary analysis of the GSWP2 baseline and sensitivity simulations indicates the range of simulated global land evaporation is ~30% of the model mean, with the COLA SSiB model (used in both GOLD products) falling on the low end of the model range. However, this is not necessarily a robust estimate of actual global land evaporation uncertainty, but continuing GSWP2 analysis will address this and be the subject of a forthcoming paper. All of these global land modeling and assimilation efforts combined with the global-scale Coordinated Enhanced Observation Project (CEOP; Leese 2001) will lead to more robust quantifications of global, continental evaporation and efforts are under way to do so.

The NVAP total precipitable water (TPW) dataset (Vonder Harr et al. 2003; Randel et al. 1996) was constructed through a blending of different products/retrievals over land and oceans from the Television and Infrared Operational Satellite (TIROS) Operational Vertical Sounder (TOVS), SSM/I, and radiosonde observations. The data are available at daily temporal resolution on a geographical 1° × 1° resolution. For the analysis that follows, monthly averaged quantities are used for the years 1988–99. The NVAP data are continually extended, updated (Vonder Harr et al. 2003), and evaluated (e.g., Amenu and Kumar 2005; Trenberth et al. 2005). Notably, Trenberth et al. (2005) in a multidataset evaluation have found important over-ocean trends in NVAP and other globally based water vapor datasets that use SSM/I-based water vapor products. Their results also imply that NVAP may have questionable quality in over-land water vapor estimates, but the lack of a "gold standard" by which to unequivocally judge the datasets remains a challenge in these types of evaluations.

b. Climate model simulation

The NASA Seasonal-to-Interannual Prediction Project (NSIPP) AGCM data were used for comparison to measure data analyses (Bacmeister et al. 2000). The model was developed for climate simulation and prediction and uses remotely sensed observations to enhance the predictability of several seasonal-to-interannual signals, notably ENSO. The model uses SST observations as ocean boundary conditions and currently maintains an output of nine ensemble runs extending from 1930 to 2000. We emphasize that the use of this data is *not to evaluate the behavior of the simulation*, but rather we use the consistency of the model-derived global quantities to elucidate the strengths and deficiencies in the disparate observationally based estimates.

TABLE 1. Annual mean global precipitation (P) and evaporation (E) fluxes (units of kg yr^{-1}) based on the period 1988–99, during which global precipitable water decreases by 2.0×10^{14} kg (see Fig. 6). For precipitation, results based on (top subrow) GPCP and (bottom subrow) CMAP are provided. For evaporation, (top subrow) GOLD and the (bottom subrow) GOLD2 land results are shown, as well as the (top subrow) GSSTF and (bottom subrow) HOAPS ocean evaporation estimates. $E - P$ using the various combinations of precipitation, land–ocean, and evaporation datasets is labeled accordingly. Error bars for the global, annual mean precipitation estimates are shown. For the global $E - P$ results, the average of GOLD and GOLD2 (denoted as "|GOLD|") are used.

	Precipitation (P)	Evaporation (E)	$E - P$
Land	GPCP: 1.05E + 17 ± 0.02E + 17	GOLD: 0.64E + 17	|GOLD| − GPCP: −4.2E + 16
	CMAP: 1.02E + 17 ± 0.02E + 17	GOLD2: 0.62E + 17	|GOLD| − CMAP: −3.9E + 16
Ocean	GPCP: 3.80E + 17 ± 0.06E + 17	GSSTF: 4.41E + 17	GSSTF − GPCP: +6.1E + 16
			HOAPS − GPCP: +1.3E + 16
	CMAP: 3.72E + 17 ± 0.04E + 17	HOAPS: 3.93E + 17	GSSTF − CMAP: +6.9E + 16
			HOAPS − CMAP: +2.1E + 16
Global	GPCP: 4.85E + 17 ± 0.06E + 17	GSSTF + |GOLD|: 5.04E + 17	(GSSTF + |GOLD|) − GPCP: +1.9E + 16
			(GSSTF + |GOLD|) − CMAP: +3.0E + 16
	CMAP: 4.74E + 17 ± 0.04E + 17	HOAPS + |GOLD|: 4.56E + 17	(HOAPS + |GOLD|) − GPCP: −2.9E + 16
			(HOAPS + |GOLD|) − CMAP: −1.8E + 16

3. Analysis

On the global scale, the water cycling "rate" may be quantified through surface evaporation fluxes to the atmosphere from the ocean and land surface or, equivalently, precipitation fluxes from the atmosphere to the surface. The atmospheric branch of the global water cycle may be expressed as

$$\frac{d\langle Q \rangle}{dt} = \langle E \rangle - \langle P \rangle, \qquad (3)$$

where the brackets represent the globally integrated total column precipitable water (Q), precipitation rate (P), and evaporation rate (E). Given this, our analysis in a strict sense is from an *atmospheric perspective*, because the disparate observationally based estimates that have been compiled (i.e., the GPCP, CMAP, GSSTF, HOAPS, and GOLD datasets) serve to evaluate the closure of (3). Other global budget equations from the perspective of the land (water storage) and ocean (salinity) can be written that encapsulate the global water cycle, and subsequently analyzed. While the near-term prospects of global satellite retrievals will allow us to address the ocean budget (discussed in more detail in the concluding section), the current global data collection of *satellite-based estimates* can only address a global water budget equation as given by (3). For some of the geographical analysis that follows, the GOLD, HOAPS, GPCP, and CMAP datasets were linearly interpolated to align all the datasets on the same 1° × 1° grid. However, to partition all the fluxes into land and ocean regions for a global budget framework, the ISLSCP land–ocean mask was used at the 1° × 1° resolution (available online at http://islscp2.sesda.com/ISLSCP2_1/html_pages/groups/ancillary/land_water_masks_xdeg.html), which is basically an aggregation of

the World Vector Shoreline data of Soluri and Woodson (1990). Based on this mapping, the global land cover area, A_{land}, is equal to 1.48×10^{14} km^2 and the global ocean cover area, A_{ocean}, is equal to 5.1×10^{14} km^2 for a total global area of 6.58×10^{14} km^2. Then, global, area-weighted averaged flux values are obtained for each flux, in their native resolution, as unit water mass per unit time per unit area (i.e., kg m^{-2} day^{-1}), noting that these units are equivalent (assuming constant water density) to the more conventional depth per unit time (i.e., mm day^{-1}). The equivalent "global" mass fluxes are then obtained by integrating the unit-area flux by the corresponding land, ocean, and global land areas. In terms of the temporal span of this analysis, overlapping all the disparate time series provide global monthly precipitation and evaporation mass flux estimates spanning the years 1988–99.

a. Annual mean and seasonality

The mean annual results are summarized in Table 1. Considering the global budget given by (3), the values of mean annual, global precipitation (both GPCP and CMAP), and evaporation estimates (using GSSTF or HOAPS) are all within ~5% of one another. By taking the mean value of the global precipitation and evaporation values obtained, a reasonable estimate of the mean annual rate of the global water cycle, based on this analysis, would be 4.8×10^{17} kg yr^{-1} or about 480 000 (metric) Gton of water. The "imbalance" (i.e., difference) between mean annual global precipitation (GPCP and CMAP) and evaporation (based on GSSTF or HOAPS) is equivalent to missing about 24 000 Gton of water (or a global mean depth of 3.65 cm), which exceeds the global precipitation error estimate. The global precipitation of GPCP is higher than CMAP for

the period of this study (1988–99), but marginally so when viewed by their error estimates. To determine the global, annual-mean error estimates of precipitation, the area-weighted mean of the monthly gridded error fields were taken, and then time averaged (and converted to a global flux). The error was then scaled by the square root of an effective number of degrees of freedom estimated from the GPCP and CMAP data (G. J. Huffman 2005, personal communication). These effective degrees of freedom (for both GPCP and CMAP) were obtained by a procedure similar to that of Schlosser and Kirtman (2005, see their appendix) and our calculation encompasses the same underlying considerations as in Janowiak et al. (1998, see their appendix A). Our technique calculates a decorrelation length scale, l, at every grid point of the data, and is based on the distance by which the temporal correlation between two grid points falls below a threshold value (in this study, we use the 99% confidence level). The median value of the gridded estimates is then taken, and a reduced resolution of "independent" grid points is then constructed as a configuration of points that are equally spaced l grid points apart in the latitude and longitude directions. The resulting degrees of freedom estimate, n, is then taken as the total number of grid points in this reduced resolution representation.

By noting in (3) that global atmospheric precipitable water variations are small compared to global flux terms (substantiated in the next section), particularly when averaged over the total span of the data (12 yr), we may write the following:

$$\langle P_l \rangle - \langle E_l \rangle \approx - (\langle P_o \rangle - \langle E_o \rangle).$$

The subscripts l and o denote the land and ocean components, respectively. The above expression reflects a quasi-consistency relation that the ocean's evaporation over precipitation excess is *approximately* balanced (i.e., to within a few percent) by the land's precipitation over evaporation excess. Stated differently, the expression represents that, on the global scale, total runoff from the continents is largely in balance with the net transport of water (vapor) by the atmosphere from over-ocean to overland regions (as also inferred, e.g., from Fig. 12.2 in Peixoto and Oort 1992). Given the values in Table 1, the disparate precipitation and evaporation data sources do not satisfy the relation very well; the mean annual values are only within ~20% for GPCP and 45% for CMAP. A (small) part of this large difference *could* be explained by a trend in water storage. However, analyses of the GOLD data indicate only very small trends in global total soil-column soil water storage (see Fig. 7 of Dirmeyer et al. 2004) as well as for any of the forcing data (not shown)

that would support any simulated trend. Furthermore, very small trends in global TPW are seen (described in the next section). However, a remarkable effect is the choice of global ocean evaporation estimate on the ocean $E - P$ diagnostic, with at least a threefold change in the global ocean $E - P$ value resulting between the use of GSSTF and HOAPS.

An additional quasi-consistency relation can also be written as

$$\langle P_l \rangle + \langle P_o \rangle \approx \langle E_l \rangle + \langle E_o \rangle.$$

This expression reflects the conception that for the annual mean global water cycle, global precipitation is almost entirely "supplied" by evaporation. As such, the ratios of the ocean and land evaporation components against global precipitation from Table 1 suggest that GSSTF ocean evaporation would account for ~91% while the HOAPS evaporation is ~76% (and continental evaporation for the remaining 9% and 24%, respectively) of global precipitation.

There also exists a robust heritage of studies that have provided estimates for annual global water cycle statistics. These studies have utilized a variety of different techniques to estimate global water fluxes and primarily use records from in situ measurements, radiosonde data, global river gauge networks, and/or reanalysis. When judged against these (Figs. 1 and 2), this study's mean annual global precipitation and evaporation fluxes fall within the previous estimates' range. Looking closer however, the legacy of estimates is characterized by the lowest values occurring in early part of the twentieth century, and among the highest values in the latter half of the twentieth century. Furthermore, the land and ocean components of evaporation and precipitation compiled from this study display considerable differences. When compared to the legacy of the studies, the GPCP and CMAP estimates from this study are among the lowest mean annual land precipitation rates (~1.0×10^{17} kg yr^{-1}). Given that the precipitation forcing was "bias corrected" with CMAP data and drove the model-based land evaporation estimate, it is not surprising that this study also provides one of the lowest land evaporation estimates (between 6.2 and 6.4×10^{16} kg yr^{-1}), particularly when viewed against the more recent estimates. Taking their residual and given the (aforementioned) negligible trends in the simulated GOLD global soil water storage, the land precipitation over evaporation excess is nearly equivalent to mean annual global river discharge. The values obtained with both the GPCP and CMAP precipitation encompass some of the more recent and explicit global river discharge estimates (e.g., Oki et al. 1999; Fekete et al. 2002; Nijssen et al. 2001). They are both slightly
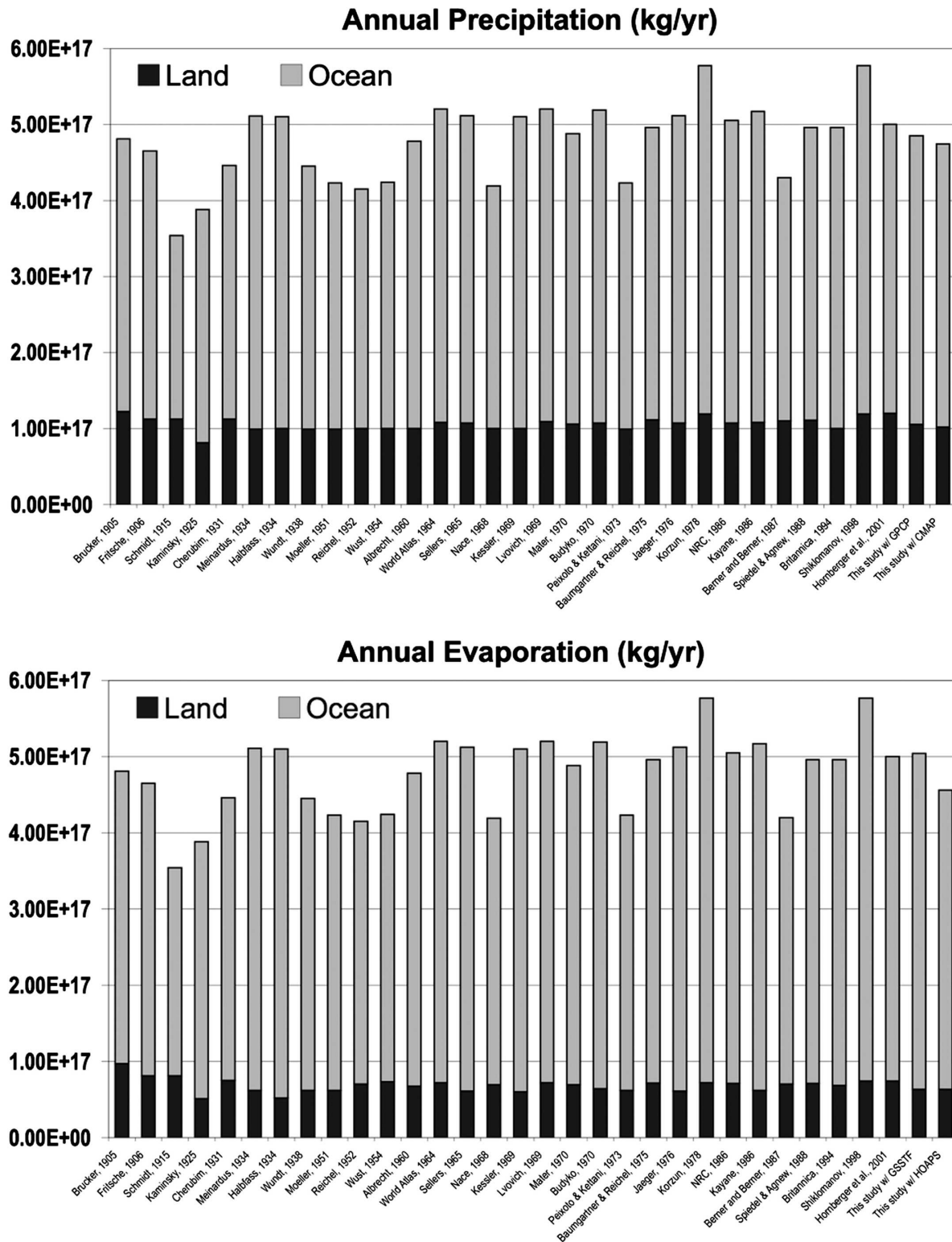
FIG. 1. (top) Mean annual *P* and (bottom) *E* as estimated by this study (using GPCP and CMAP data) and taken from a selection of previous publications. All estimates prior to 1970 were selected for this figure from the survey done by Korzun (1978), and explicit references of those studies are contained therein. In this adaptation of the Korzun survey, only the most recent estimate from each author is considered.
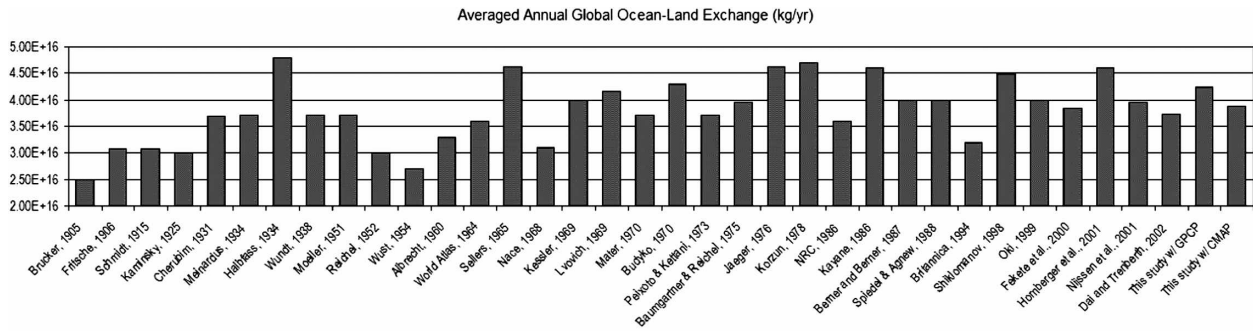
FIG. 2. Mean annual water exchange between the ocean and land (via atmospheric transport or river discharge) as estimated by this study and prior studies. As in Fig. 1, estimates prior to 1970 are selected and adapted for this figure from the survey of Korzun (1978).

higher than the most recent and quite comprehensive estimate obtained by Dai and Trenberth (2002)—given as $37\,288 \times 10^{16} \pm 662 \times 10^{16}$ kg yr^{-1}. Given this, the CMAP estimate falls marginally outside the error range $(= \pm 2\%)$. However, the error obtained by Dai and Trenberth (2002) was estimated based on a root sum-squared variance of long-term annual flows from 921 rivers, and then scaled by an empirical coefficient (that translates station flows to river mouth flows). Therefore, it is quite likely that this error estimate has some degree of uncertainty as well, particularly when viewed against the conventional wisdom that most streamflow records are accurate to within 10%–20% (Fekete et al. 2002). Given all these considerations, we must call into question the $P - E$ rates obtained for the ocean (Table 1), and thus are either caused by deficiencies in precipitation and/or evaporation estimates over the ocean. The analysis in a later section (3c) will indicate that it is likely caused by uncertainties regarding the ocean evaporation estimates.

Looking closer at the legacy of global river discharge estimates, some notable characterizations can be made. First, the lowest and highest estimates of global river discharge are seen in the earlier published studies (i.e., in the first half of the twentieth century). In the latter half of the twentieth century, the scatter among the estimates of annual global river discharge is smaller. However, generally speaking the annual mean discharge scatter exceeds the interannual global river discharge variability. Based on a continuous annual global runoff time series by Korzun (1978) that spans the years 1918–67, the annual global runoff standard deviation is 1.25×10^{15} kg yr^{-1}. However, the standard deviation of the annual mean values documented over the same time period (1918–67, as given by Fig. 2) is 4.4×10^{15} kg yr^{-1}. During the latter half of the twentieth century, this characterization does not improve much. From 1966 to this study, the standard deviation of the pooled annual mean estimates is 4.3×10^{15} kg yr^{-1}, while the

global river discharge standard deviation based on Global Runoff Data Center (GRDC) records for the years 1986–95 (Fekete et al. 2002; Fekete et al. 1999) is 2.1×10^{15} kg yr^{-1}. The GRDC global runoff data are based on a blend of 390 station observations with model calculations that cover the major global river basins. In calculating its standard deviation of interannual variations, the annual discharge data were detrended (based on a least squares, linear regression fit). The detrended value is lower than the standard deviations obtained in this study (two uppermost, right-hand cells in Table 2).

The global geographic $P - E$ distributions (Fig. 3) reveal some important characteristics. First, the continental regions are dominated by excess precipitation, as expected. Furthermore, continental regions showing an excess of evaporation to precipitation are found in the major desert regions of Africa (northern Sahel region and the southern part of the Saharan Desert region) as well as the tundra region of the Tibetan Plateau, again as one would intuitively expect. The regions of maximum evaporation excess are confined to the subtropical ocean regions (for all data combinations). The tropical ocean regions are characterized by an abrupt shift to substantial excess precipitation. This is consistent with the coincidence of the ITCZ and relative minima evaporation rates (cf. Seager et al. 2003). The distinctions between the GPCP- and CMAP-derived fields are seen mostly in the extratropics. The GPCP result gives a greater precipitation excess over most of the continental regions (consistent with the greater $P - E$ value over land in Table 1), and the CMAP field indicates weaker precipitation excess (or a reversal to evaporation excess) compared to GPCP's precipitation excess over extratropical oceans (consistent with larger negative values of $P - E$ over the ocean in Table 1). The most salient differences between the use of the GSSTF and HOAPS ocean evaporation datasets are seen largely in the subtropics. The largest changes (i.e., decrease from GSSTF to HOAPS) are found in the sub-

TABLE 2. Std devs of annual mean (1988–99) global precipitation (P) and evaporation (E) mass flux statistics. For precipitation, the results based on (top subrow) GPCP and (bottom subrow) CMAP are provided. For evaporation, boldface indicates that the detrended (linear, least squares fit) global, annual ocean evaporation time series was used for the calculation (kg yr^{-1}).

	Precipitation (P)	Evaporation (E)		$E - P$
Land	GPCP: 2.9E + 15	GOLD1: 0.7E + 15		|GOLD| − GPCP: 3.1E + 15
	CMAP: 3.1E + 15	GOLD2: 0.8E + 15		|GOLD| − CMAP: 3.2E + 15
Ocean	GPCP: 5.9E + 15	GSSTF: 2.15E + 16	**6.3E + 15**	**GSSTF − GPCP: 5.5E + 15**
				HOAPS − GPCP: 8.3E + 15
	CMAP: 5.0E + 15	HOAPS: 1.48E + 16	**1.0E + 16**	**GSSTF − CMAP: 5.2E + 15**
				HOAPS − CMAP: 1.2E + 16
Global	GPCP: 6.3E + 15	|GSSTF + GOLD|: 2.2E + 16	**6.5E + 15**	**(GSSTF + |GOLD|) − GPCP: 5.8E + 15**
				(GSSTF + |GOLD|) − CMAP: 5.7E + 15
	CMAP: 5.7E + 15	|HOAPS + GOLD|: 1.5E + 16	**1.0E + 16**	**(HOAPS + |GOLD|) − GPCP: 0.7E + 15**
				(HOAPS + |GOLD|) − CMAP: 1.0E + 16

tropical South Pacific and Atlantic Oceans. The use of the HOAPS estimates also leads to a more homogenous global pattern of $P - E$ (weaker highs and lows) as compared to the GSSTF result (middle and bottom panel of Fig. 3).

Looking at the mean annual cycles of the global water fluxes, several characterizations can be made when viewed against the annual mean cycle of TPW changes. The GPCP and CMAP mean annual cycles (Fig. 4, top panel) have significant differences (when judged by their error estimates). CMAP gives larger precipitation rates for June (marginally) and July, while GPCP has larger precipitation rates for February, March, and October–December. Given these distinguishing differences, CMAP displays a modest seasonality, with its highest rate in July and lowest in February. Aside from the low February rate, GPCP shows no well-defined seasonality. However, regardless of these differences, the resulting amplitudes of the global $E - P$ annual cycles (Fig. 4, bottom panel), using any combinations of the data, are considerably larger than what the monthly global TPW changes would suggest. The most excessive global $E - P$ amplitude results using GPCP and GSSTF data. However, the GPCP/GSSTF results are also able to achieve more consistent values (with respect to the TPW changes) during the Northern Hemisphere winter months. Looking at the HOAPS estimates, while lower amplitudes (cf. GSSTF/GPCP) of the global $E - P$ annual cycle result, the robust low bias of the HOAPS estimate (relative to the GPCP and CMAP precipitation fields) is clearly evident.

The zonal features of the annual cycle of $E - P$ (Fig. 5) show a modest sensitivity to the choice of data used. However, for all data configurations, high-latitude and equatorial precipitation excess as well as subtropic and low- to midlatitude evaporation excess (with a modest Northern Hemisphere seasonality) is seen. The intertropical convergence zone (ITCZ) progression is also

quite evident. The most distinguishing differences between the GPCP- and CMAP-derived estimates are that the CMAP field shows weaker atmospheric drying (i.e., negative $E - P$) at high latitudes, but more ubiquitously stronger atmospheric drying in the Tropics. These results are in good agreement with the zonal differences in GPCP and CMAP shown by Yin et al. (2004, their Fig. 4). The most pronounced effect of replacing GSSTF with the HOAPS data is a rather ubiquitous weakening of evaporation excess. Furthermore, the use of GSSTF with GPCP results in a substantial weakening of $E - P$ seasonality in the northern subtropics.

b. Interannual variability

While the closure between disparate estimates of mean annual global precipitation and evaporation is reasonable, their year-to-year changes (Fig. 6) reveal more notable discrepancies. The correlations between interannual global precipitation (GPCP or CMAP) and global evaporation (GSSTF or HOAPS plus estimated continental evaporation) variations are quite low (ranging from 0.44 to −0.6), and even if the GSSTF annual data trend is removed (through a linear, least squares fit), the correlation increases to only as high as 0.59 for GPCP and 0.34 for CMAP (both with GSSTF-based global evaporation). Similar results are seen for correlation between monthly variations. This is in contrast to the AGCM simulations, where the interannual global precipitation and evaporation estimates show a very strong correlation (0.95). Moreover, observed global TPW changes cannot account for the trend or interannual variability in global precipitation and evaporation differences. The year-to-year changes in mean January global precipitable water, shown in Fig. 6, are on the order of 10^{13} kg yr^{-1}, and the time series is quite consistent with other recent global analyses conducted (e.g., Amenu and Kumar 2005; Trenberth et al. 2005).
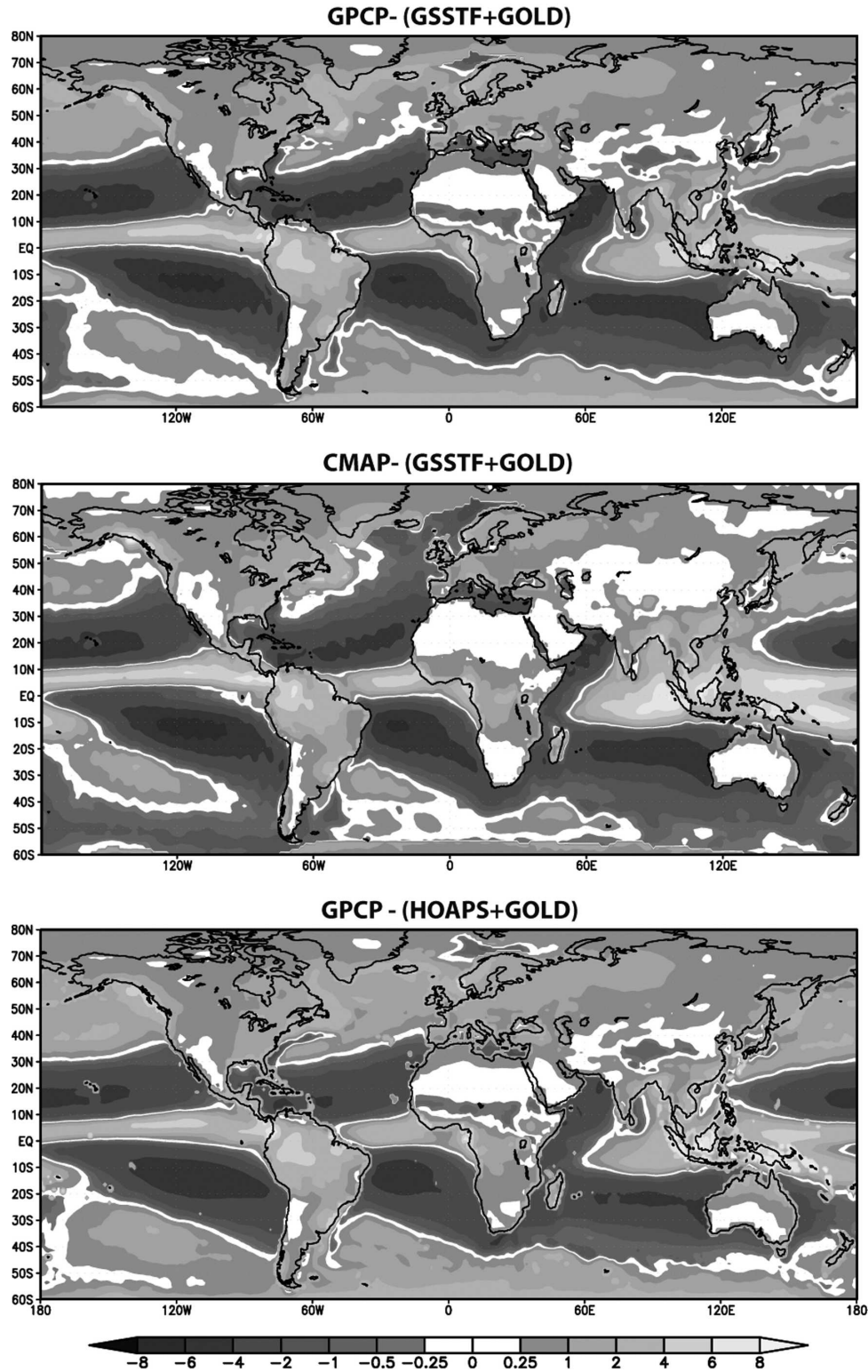
FIG. 3. Global distribution of the annual mean (1988–99) difference between P and E (mm day^{-1}). (top) The field obtained using GPCP precipitation and GSSTF + GOLD evaporation, (middle) the result with CMAP precipitation and GSSTF + GOLD evaporation, and (bottom) the result for CMAP precipitation and HOAPS + GOLD evaporation.
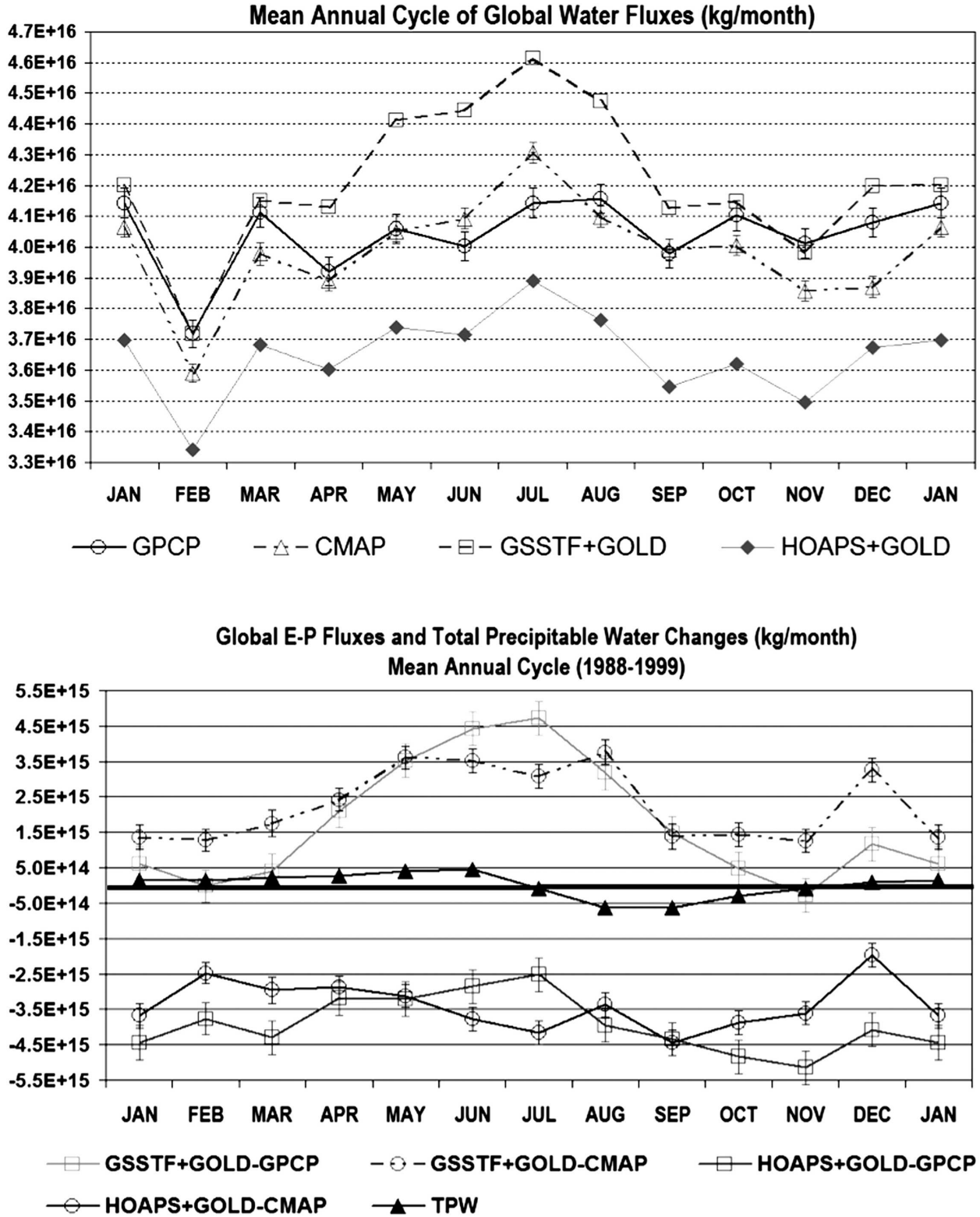
FIG. 4. Mean annual cycle of global water fluxes and total precipitable water changes based on the 1988–99 period of (top) data and (bottom) $E - P$ and TPW changes. Global estimates of precipitation (the GPCP and CMAP data) and evaporation (using GOLD, GSSTF, and HOAPS) are described in text. Error bars are provided for the global precipitation estimates, and represent the area-weighted, global average of the gridded random error estimates (scaled by the effective degrees of freedom.
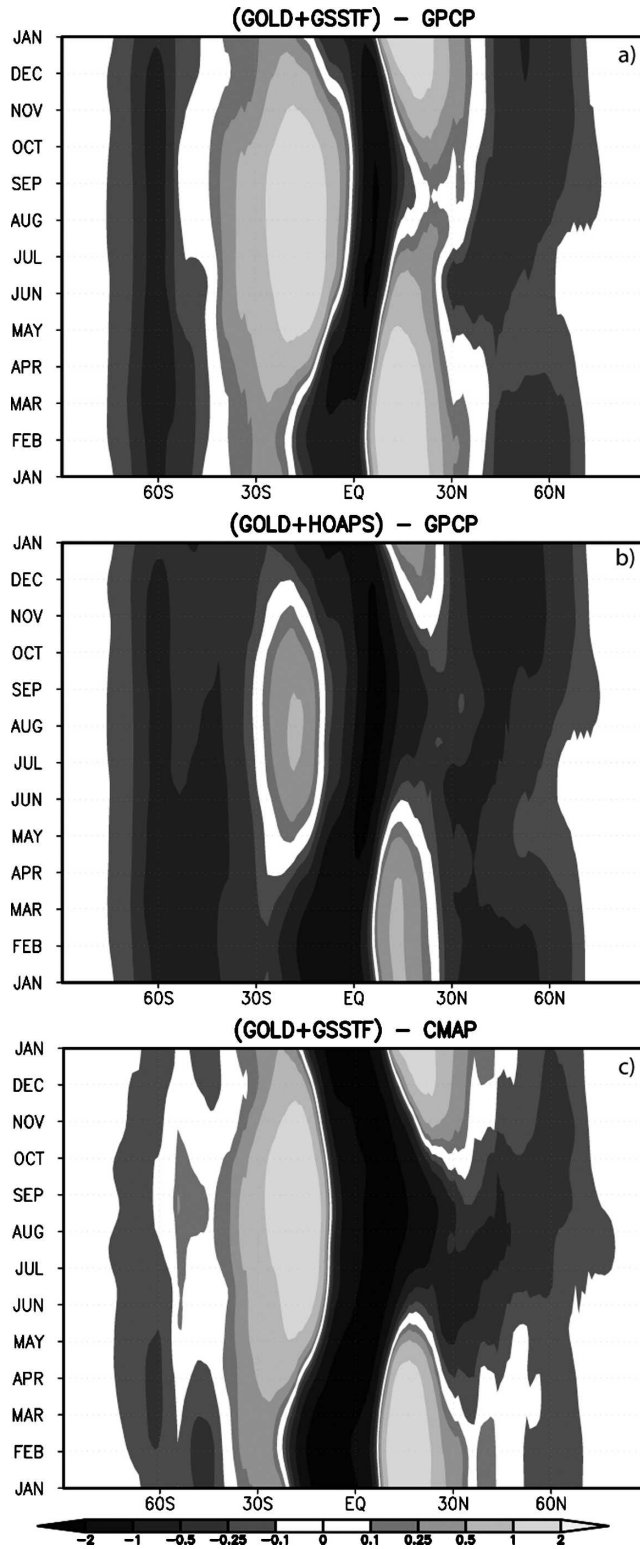
FIG. 5. Averaged annual cycles of zonally integrated evaporation (based on GSSTF, HOAPS, and GOLD data) minus precipitation (based on GPCP or CMAP). Units are in 10^{13} kg day^{-1}. Compared to (c), the (GOLD + HOAPS) − CMAP result (not shown here) depicts the identical differences seen between (a) and (b).
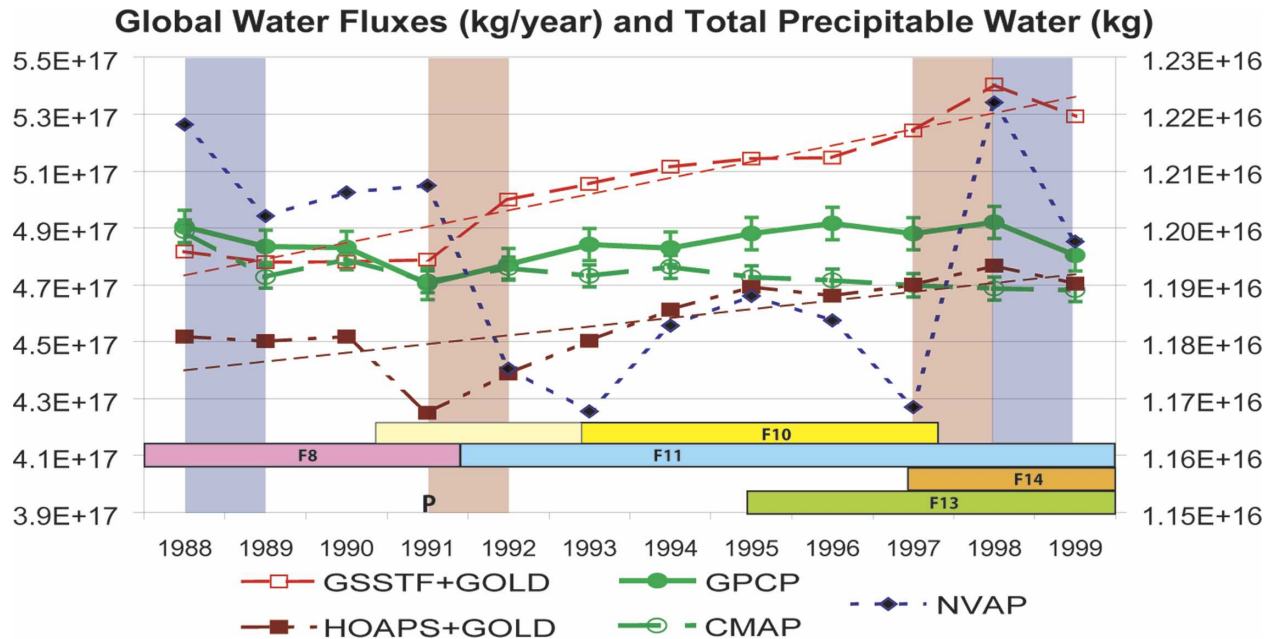
Global Water Fluxes (kg/year) and Total Precipitable Water (kg)

FIG. 6. Annual time series of global water fluxes and TPW. Global estimates of precipitation (the GPCP and CMAP data), evaporation (the GOLD, GSSTF, and HOAPS data), and TPW are described in text. The left axis denotes water flux values and the right axis depicts the scale of TPW estimates. The light dashed line denotes the linear (least squares) fit to the global evaporation trend. Error bars are provided for the global precipitation estimate, and represent the area-weighted, global average of the gridded random error estimates—scaled by the effective degrees of freedom. The shaded bars at the bottom of the frame denote the time sequence and durations of all the SSM/I missions (upon which the GSSTF and HOAPS ocean evaporation estimates are based). The lighter shade of yellow denotes the period in which the F10 SSM/I was in orbit, but data were not used for the NVAP estimates. The vertical red and blue bars indicate where year-to-year changes coincided with an El Niño or La Niña, respectively. The location of the bold "P" indicates the approximate timing of the Mt. Pinatubo eruption (15 Jun 1991).

However, the annual, global $E - P$ rates are on the order of 10^{15} kg yr^{-1} (even if not considering the evaporation trend). Moreover, given the precipitation error bars, the $E - P$ rates could not achieve an accuracy that would explain the annual TPW changes. The disparity between estimated $E - P$ and TPW is unlike the substantially tighter (mass balance) agreement for the respective AGCM interannual and monthly variations (not shown). Moreover, global TPW is typically on the order of 10^{16} kg, and therefore most of the annual global $E - P$ values (also on the order of 10^{16} kg yr^{-1}) indicated by Fig. 6 are unacceptable. It should be noted that estimates of TPW error are absent from this discussion. However, our use of the NVAP data was to illustrate the order of magnitude consistency that should be seen in the global water fluxes. As we show, the global, annual water vapor changes are about two orders of magnitude lower than annual $E - P$ rates. So the acceptance of these annual, global water vapor changes as relative "truth" would be invalid only if the water vapor error was about two orders of magnitude larger than its annual variation (shown in Fig. 6); this is very unlikely.

The GPCP and CMAP global, annual precipitation estimates are seen to be consistent (i.e., within their error range) for the years 1988–94, with the exception of a marginal difference (just outside the error range) in 1993. Their values diverge considerably during the period 1995–98, with a rebound tending to a more consistent value in 1999 (though their values are still outside the uncertainty overlap). However, the most notable feature of the annual mean time series is the overall trend seen in global evaporation. The trend rate is ~1% yr^{-1} using the GSSTF data, and ~0.5% yr^{-1} for the HOAPS result. These trends are solely caused by these ocean evaporation estimates, which are derived mostly from SSM/I-retrieved fields.

There is a notable correspondence between the larger jumps (i.e., increases) in the global evaporation estimates and major transitions between SSM/I instruments (e.g., Colton and Poe 1999), the most notable being the transition between F8 and F11 (beginning of 1992) and the period during and just after the overlap of the F10, F13, and F14 missions (the F11 mission was also operational). Further, some of the largest jumps in the NVAP TPW estimate also correspond closely with
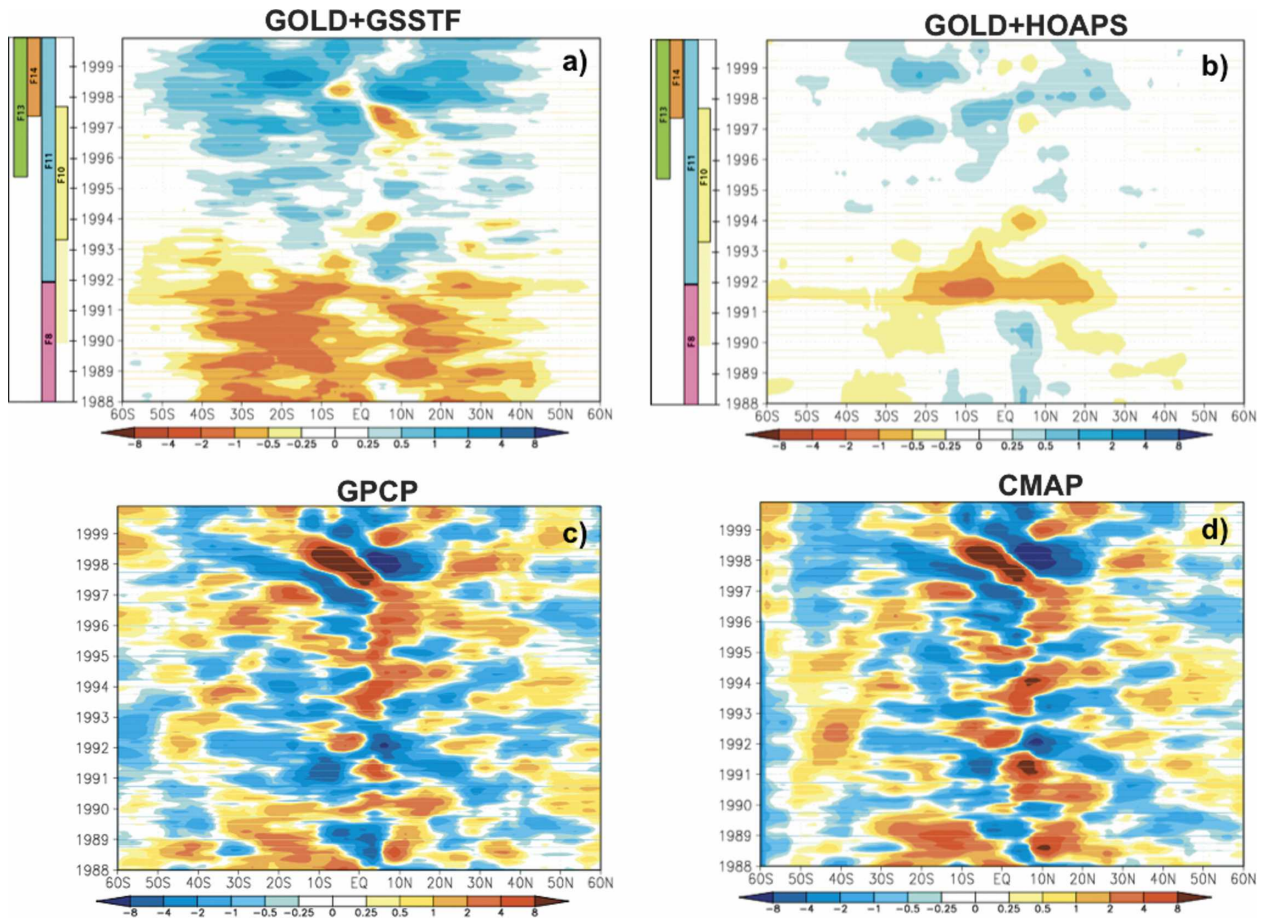
FIG. 7. Monthly zonal integrated anomalies of (a) GOLD + GSSTF evaporation, (b) GOLD + HOAPS evaporation, (c) GPCP precipitation, and (d) CMAP precipitation. The data are temporally smoothed by performing a running 6-month average (10^{12} kg day^{-1}). In (a) and (b) the shaded bars to the left of the frame denote the time sequence and durations of all the SSM/I missions (upon which the GSSTF ocean evaporation estimates are based). The lighter shade of yellow denotes the period in which the F10 SSM/I was in orbit, but data were not comprehensively used.

the noted SSM/I transitions, but show no unambiguous consistency with the large global evaporation increases (the only consistent change is from 1997 to 1998). Furthermore, the substantial changes in the processing of the NVAP retrieval starting in 1993 (Vonder Harr et al. 2003) show no discernable effects to the subsequent global TPW values. As shown in Fig. 6, the large increases in evaporation and TPW in 1998 as well as the substantial changes in 1992 are likely a compounded result of a SSM/I transition, ENSO and (for 1992) the Mt. Pinatubo eruption (also discussed in Amenu and Kumar 2005; Trenberth et al. 2005). All but the large decrease in TPW between 1991 and 1992 is consistent with ENSO events (i.e., El Niño causes an increase and La Niña a decrease), but this is probably also affected by the subsequent global cooling of the Mt. Pinatubo eruption (Soden et al. 2002).

The anomalies of $E - P$ exhibit distinct patterns dur-

ing El Niño and La Niña events. The most discernable feature associated with an El Niño is prominent evaporation excess in the northern Tropics and precipitation excess in the southern Tropics. These excesses are a result of complementary evaporation and precipitation anomalies, although the precipitation anomalies are much stronger (Fig. 7). The analysis also suggests that the locations of the precipitation and evaporation excess are reversed prior to El Niño. In particular, the 1998 event finds the precipitation excess, in effect, "flanked" by evaporation excess that occurs just north of the equator in the winter prior to an El Niño and then propagates southward (and subsequently replaced by the precipitation excess). The La Niña patterns are not quite as prevalent, but in the two that occur during the data time span, weaker anomalies of opposite sign to those seen during an El Niño occur. All of these ENSO-related $E - P$ features, which are largely a re-

flection of precipitation anomalies, are consistent with documented climatological equatorial precipitation behavior associated with ENSO (e.g., Diaz et al. 2001; Curtis et al. 2001).

c. Diagnosis of evaporation trend

The analysis (Fig. 6) indicates a substantial ~0.5%–1% yr^{-1} global evaporation trend. Although global summed land and ocean evaporation is shown in Fig. 6, the trend is exclusively caused by the GSSTF and HOAPS ocean evaporation estimates. Furthermore, no complementary global precipitation trend is observed, and perhaps just as important, the global evaporation trend falls outside the GPCP and CMAP precipitation error bars. As previously mentioned, global precipitation error bars are calculated in Fig. 6 as the globally averaged (area weighted), annual average of the monthly gridded values—scaled by the effective degrees of freedom of the GPCP and CMAP data. As such, the errors of the global GPCP and CMAP estimates would preclude the global evaporation trend—given that the GCM and TPW results indicate precipitation and evaporation, variations should be consistent within the precipitation error range. Inspection of the NSIPP AGCM simulation indicates that global evaporation and precipitation trends (not shown) exist, but they are an order of magnitude smaller (~0.1% yr^{-1}) than the observed ocean evaporation trend. Moreover, recent analysis (e.g., Räisänen 2002; Allen and Ingram 2002) from the Coupled Model Intercomparison Project (CMIP) of global evaporation trends in transient CO_2 experiments using global, fully coupled climate models also show trends that are (at least) an order of magnitude smaller. The NSIPP AGCM simulated global precipitation and evaporation trends are also substantially more consistent than the observed trends, which is consistent with their strong temporal correlation (noted in the previous section). Qualitative inspection of the CMIP results also indicates a similar, tight consistency in the global evaporation and precipitation trends. An additional analysis result that highlights the inconsistency between the observed trends is a lack of an observed TPW trend. If global evaporation was increasing with steady global precipitation, global TPW should also increase to store the excess evaporation. While recent evidence indicates that a ubiquitous increase in TPW (based on SSM/I retrievals alone) is likely to have occurred during the period considered here over most oceans (e.g., Trenberth et al. 2005), it is not globally evident.

These findings suggest the leading explanation of the above-mentioned discrepancies are likely attributed to the global evaporation trend. The GSSTF trend is ap-

proximately twice that of HOAPS (Fig. 6), and we therefore focus our attention to the GSSTF trend. In doing this, we view the factors contributing to the GSSTF ocean evaporation trend to be stronger yet similar with that of HOAPS—as both datasets largely rely on SSM/I retrievals. The evaporation trend signature is most evident (especially for GSSTF) in Southern Hemisphere subtropical regions (Fig. 7). Further diagnosis was performed to explore the ocean evaporation trend source, based on its bulk aerodynamic formulation given by (1). The two main inputs to the formulas, $(Q_s - Q_a)$ and $|V|$ both show discernable trends (Figs. 8 and 9 shows GSSTF's humidity terms separately). As such, the trends of winds and humidity gradient are then multiplied within the bulk aerodynamic algorithm. It is therefore not surprising to see a robust ocean evaporation trend as a result, particularly for the GSSTF product. The near-surface wind patterns of GSSTF (Wentz and Schabel 2000) and HOAPS (Bentamy et al. 1999) are similar, even though both are derived from different retrieval approaches (described in section 2). The trend in Q_a is much stronger for GSSTF. Overall, Q_s patterns (Fig. 9 for GPCP, but HOAPS not shown) are generally similar, even though different data and procedures are used for the Q_s estimate. HOAPS uses SSTs based on a subsampling of the Pathfinder Advanced Very High Resolution Radiometer (AVHRR) data (Bentamy et al. 2003), while the GSSTF estimate uses SSTs based on the NCEP–NCAR reanalysis (Chou et al. 2003). The NCEP–NCAR SSTs are taken from the Reynolds and Smith (1994) data, and furthermore, this product is used to constrain the Pathfinder AVHRR product.

The only substantial impact of the Q_s differences is a dramatic drop in the HOAPS near-surface humidity gradient (Fig. 8) seen in the wake of the Mt. Pinatubo eruption (i.e., the year following 1 June 1991). This is a result of the HOAPS usage of AVHRR Pathfinder SST data (Fig. 10), which does not correct for aerosol effects. This causes a substantial drop in the HOAPS evaporation estimate throughout the Tropics for the remainder of 1991, with subtropical features persisting well into 1992, and South Pacific tropical anomalies lasting into 1993. None of these features are seen in any of the corresponding GSSTF fields. GPCP's substantial decreases during 1991 (Fig. 7) do not clearly align with the Pinatubo eruption. Furthermore, the GPCP anomalies following the Pinatubo eruption show a dominating El Niño response. Nevertheless, ongoing analyses with the GPCP product indicate that a (second order) volcanic signal in the GPCP data can be extracted through careful temporal filtering (R. F. Adler 2005, personal communication).
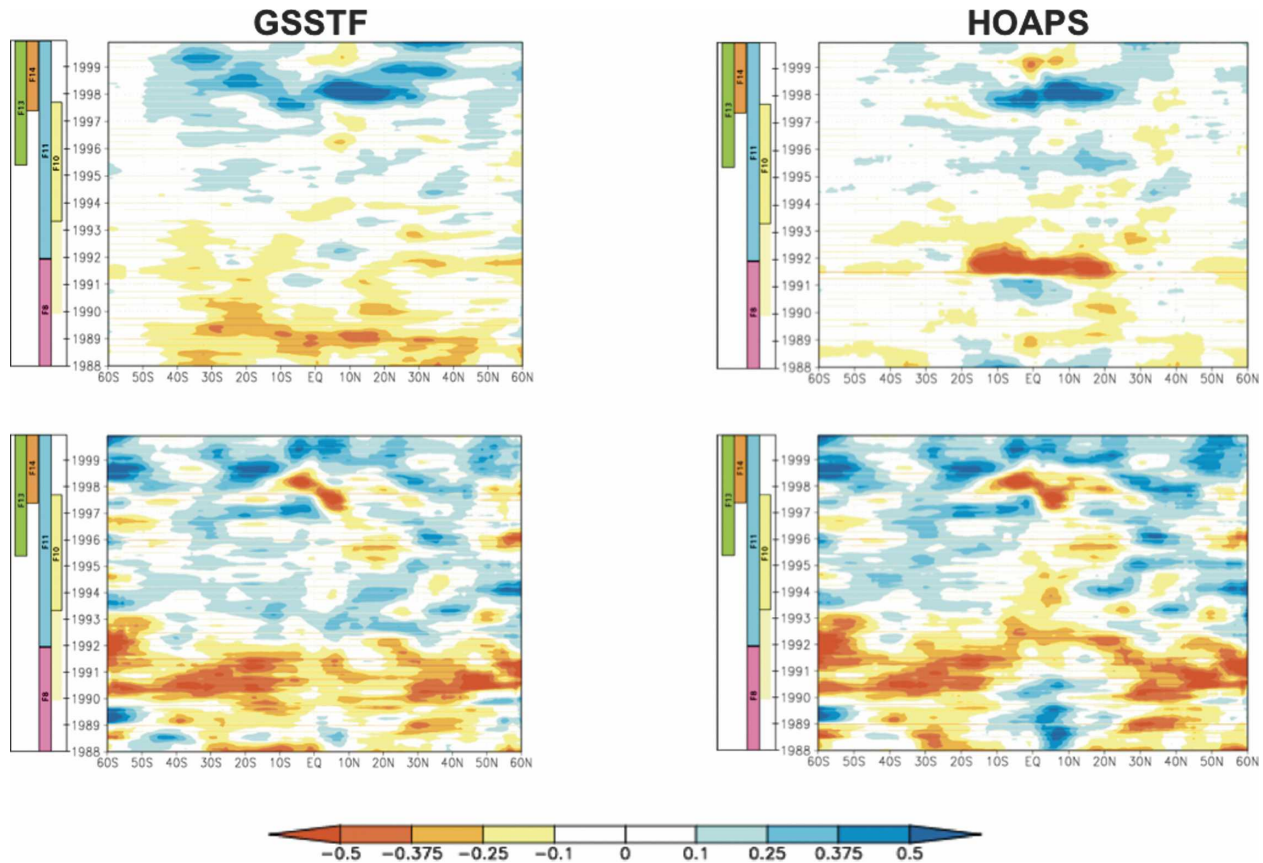
FIG. 8. Monthly zonal averaged (top) $Q_s - Q_a$ and (bottom) near-surface wind speed time series anomalies. The data are temporally smoothed by performing a running 6-month average (g kg^{-1} and m s^{-1}). The shaded bars to the left of each frame denote the time sequence and durations of all the SSM/I missions.

Looking more closely at the wind anomalies (Fig. 8), the shift (from negative to positive) in the overall wind anomaly sign occurs during 1992—this is in striking correspondence with the transition between the F8 and F11 SSM/I instruments. This shift in the SSM/I wind speed is also consistent with the Meissner et al. (2001) analysis (see their Fig. 1). This shift is preceded by the most extensive positive wind speed anomaly (that persists through 1990 and most of 1991). Near the end of the record, wind anomalies maintain their strongest negative anomalies, and the onset of this period closely corresponds to the phasing out of F10 and the beginning of F14's operation. One encouraging feature of the wind speed record is the strong negative anomalies about the equator that are coincident with the 1997/98 El Niño (consistent with the breakdown of the trade winds).

For the humidity gradients, further analysis of GSSTF's individual terms Q_s and Q_a (Fig. 9) shows a heterogeneous mixture of anomalies and trends, which results in the more uniform evolution of its $Q_s - Q_a$

trend (Fig. 8). The end of the persistent negative Q_a anomaly in 1992 (primarily in the subtropical Southern Hemisphere) is similar to wind speed in that it corresponds closely to the F8–F11 transition. Overall, the negative Q_a trend is consistent with the positive estimated ocean evaporation trend. However, the correspondence of any shift or change in Q_a to the F10/F14 transition period is subtle. In fact, most of the interannual Q_a anomaly features consistently follow the SST anomalies, as expected (Fig. 10). Near the end of the record, the midlatitude consistency between SST and Q_a is absent, and may be, in part, the background negative trend (corresponding to SSM/I transitions) dominating any other signal. The consistency of Q_s anomalies, as opposed to Q_a, to SSTs is much stronger, as expected (bottom panels of Figs. 9 and 10). Generally speaking, a gradual trend in Q_s is not prevalent (as opposed to Q_a). Nevertheless, the strong positive Q_s anomalies prevalent near the end of the record support the positive ocean evaporation trend estimate.

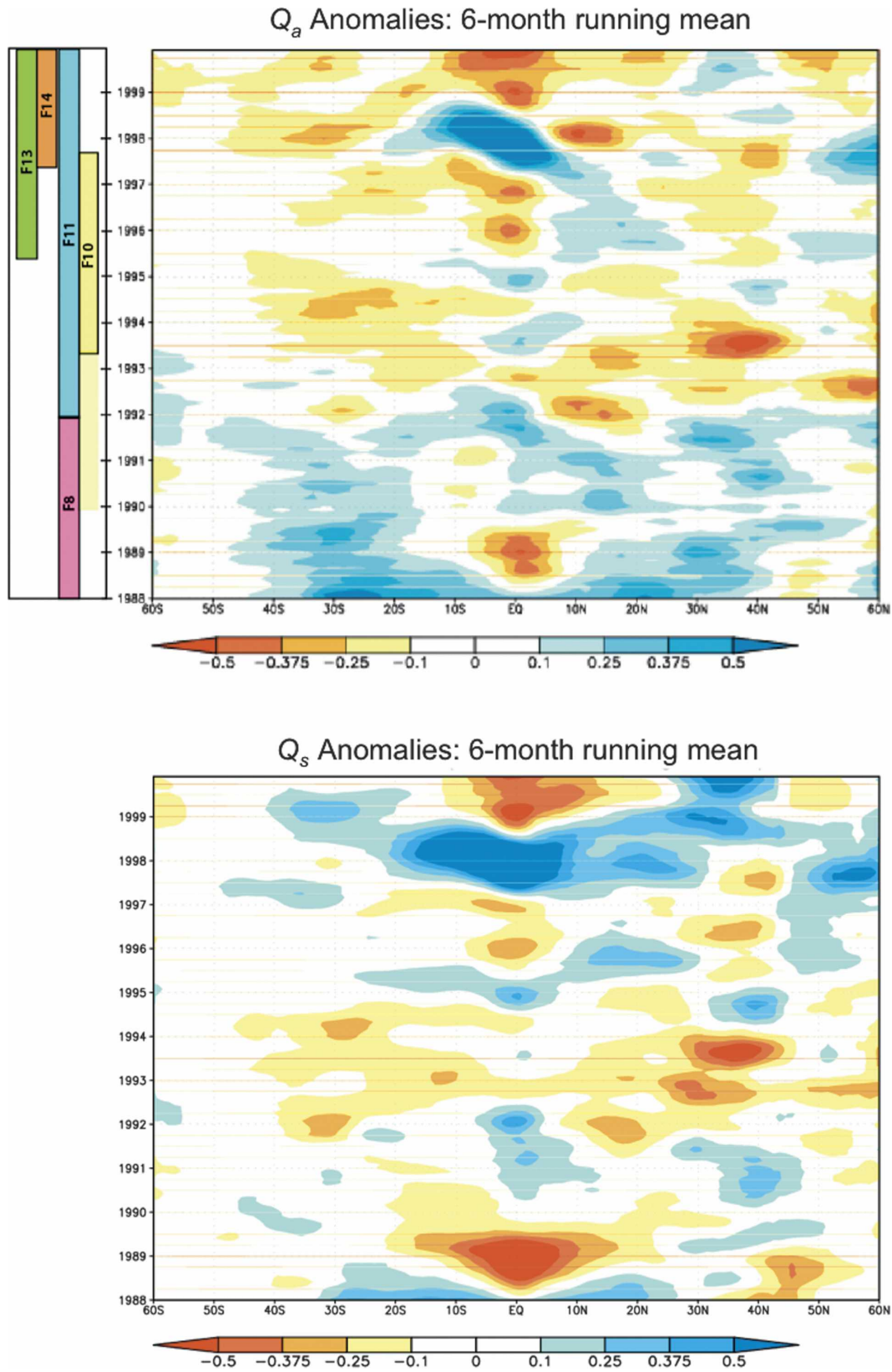According to Chou et al. (1995, 2003), the GSSTF

Q_a Anomalies: 6-month running mean

Q_s Anomalies: 6-month running mean

FIG. 9. Monthly zonal averaged (top) Q_a and (bottom) Q_s time series anomalies based on the GSSTF data. The data are temporally smoothed by performing a running 6-month average (g kg^{-1}). The shaded bars to the left of the top frame denote the time sequence and durations of all the SSM/I missions.
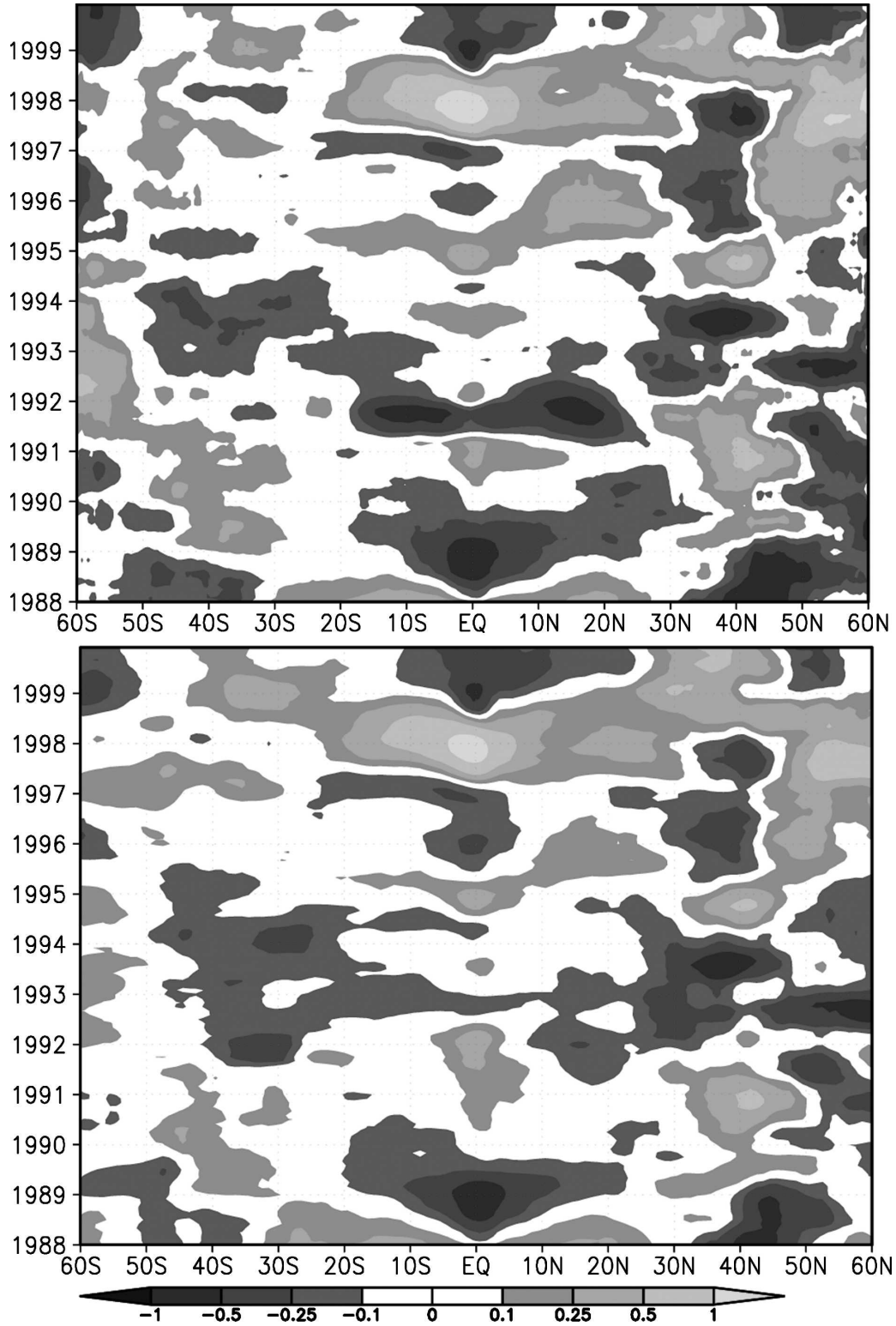
FIG. 10. Monthly zonal averaged SST time series anomalies based on (top) the HOAPS Pathfinder sampling and (bottom) NCEP–NCAR reanalysis. The data are temporally smoothed by performing a running 6-month average (K).

approach uses retrieved Q_a and wind speed estimates based on SSM/I data. For Q_s, its value was derived from SST estimates that were provided from reanalysis. It is therefore not surprising that a gradual trend with a distinct sign shift in 1992 are seen in both Q_a and wind speed, and that Q_s does not show the same degree of qualitative similarity. Both S.-H. Chou (2002, personal communication) and Curry et al. (2004) emphasize the importance of the SST data quality, and the discrepancies found in this analysis between HOAPS and GSSTF in the wake of the Pinatubo eruption underscore this point. However, the presented analysis would indicate that the ocean evaporation trend, based on a bulk aerodynamic formula, is largely a manifestation of SSM/I-based wind and humidity products used in (1). As such, these products must be carefully reinspected to find the extent and cause of the apparent intersensor disjoints in the data, particularly for the F8–F11 transition and F10–F13 overlap period.

4. Summary and conclusions

In summary, an analysis of global satellite-based precipitation and evaporation estimates indicates that on an annual-averaged basis, the imbalance of global precipitation and evaporation estimates is about 5%, and exceeds the estimated uncertainty of global mean annual precipitation ($\sim\pm1\%$). However, for any given year, the annual mean flux imbalance can be as high as 10% (i.e., on the order of 10^{16} kg yr^{-1}), but the total precipitable water interannual variations suggest that the agreement should be as low as 0.01% (i.e., $\sim 10^{13}$ kg yr^{-1}). The correlation between observed interannual global precipitation and evaporation variations are quite low (between 0.59 and 0.34, untrended), in contrast to an AGCM simulation (0.95). The observed global total precipitable water (TPW) changes cannot account for the trend or variation differences between any of the global precipitation and evaporation estimates. Moreover, global TPW is typically on the order of 10^{16} kg, and therefore the annual global $E - P$ values (also on the order of 10^{16} kg yr^{-1}) indicated are highly unlikely. The analysis also suggests that substantial, but excessive, trends of $\sim 0.5\%$–1% yr^{-1} exist in the global ocean evaporation estimates considered. Qualitatively, this trend direction is consistent with the AGCM simulation, but the AGCM trend is an order of magnitude smaller. The largest increases in annual ocean evaporation are in close correspondence with transitions between SSM/I instruments, from which retrieved near-surface atmospheric humidity and wind speed are used for the bulk estimate. In spite of the potential deficiencies noted above, an average global

water cycling "rate" equal to the global, annual-averaged precipitation or evaporation derived from this analysis is equal to 4.80×10^{17} kg yr^{-1} with at least an uncertainty of $\pm 0.05 \times 10^{17}$ kg yr^{-1} (the averaged GPCP and CMAP global error) and a standard deviation of 7.1×10^{15} kg yr^{-1}.

As previously noted, a consistency assessment of our global freshwater discharge, (i.e., $P - E$ over land) combined with our ocean $E - P$ estimates against observed ocean salinity is absent. Ocean evaporation enhances dissolved salts that increase salinity and likewise, precipitation dilutes the saltiness of the upper-ocean layers. Salinity tends to be high in midlatitudes where evaporation is high and lower near the equator where precipitation is high. Very high latitudes can also see decreases in salinity where sea ice is melting, and decreases in salinity is expected near river outlets. Curry et al. (2003) presents a comparison of salinities on a long transect (50°S–60°N) through the western basins of the Atlantic Ocean between the 1950s and the 1990s, finding a systematic freshening at both poleward ends contrasted with large increases of salinity pervading the upper water column at low latitudes. These large increases of salinity at low latitudes correspond to an increase of 5%–10% in evaporation over the 40-yr period. Scientific progress in using salinity to diagnose global evaporation, precipitation, and runoff changes is limited because conventional in situ salinity sampling is too sparse to give the global view of salinity variability. While substantial improvements and updates in the global salinity archive has become available (e.g., Conkright et al. 2002), its temporal and spatial coverage allow for only long-term analysis (i.e., over multiple decades) of multiyear averages (e.g., Boyer et al. 2005). Present-day salinity observations are very sparse, with 25% of 1° latitude–longitude squares devoid of measurements and >73% with fewer than 10 observations (Koblinsky et al. 2003). Two satellite missions are now being developed to provide the first synoptic global salinity observations on a weekly to monthly time scale, and spatial resolutions on the order of 100 km. Analysis of these forthcoming salinity observations should provide great insight on changes in the trends and variations of the global water cycle. As with the spatial and temporal sampling of satellite-retrieved surface salinity, complemented by the continuing measurements from ship and buoy data, a more cohesive collection of ocean salinity data will be available and allow for a more consistent and seamless application to the type of analyses conducted in this study.

Several implications for observational global water cycle capability, accuracy, and consistency result from this study. Based on the analyses' estimated global

GPCP and CMAP annual precipitation variabilities (i.e., the global values in Table 2), a monotonic global precipitation increase of at least 0.3% yr^{-1}, over the length of this data synthesis (12 yr) would be required for "low-risk" linear-trend detection. This low-risk minimum trend value was obtained by using Eqs. (1)–(3) in Ziegler et al. (2003) with α and β values deemed low risk and solving for $|\tau_{min}|$. The solution for $|\tau_{min}|$ is fairly insensitive to the choice of using GPCP or CMAP (resulting minimum trend values are within 0.03% yr^{-1} of each other). However, this minimum trend estimate does not explicitly account for measurement error, and thus the degree of uncertainty in the global annual GPCP and CMAP estimates (i.e., ranges given in Table 1 and the error bars in Fig. 6) would imply a stronger trend needed for minimal detection. Nevertheless, recent multimodel analysis of global change simulations from CMIP2 (Räisänen 2002) show a range of global precipitation changes of −0.2%–5% as a result of transient (1% yr^{-1} increase during an 80-yr simulation) doubled-CO_2 concentrations. In terms of annual rate precipitation trends, this CMIP2 range translates to approximately −0.003%–0.07% yr^{-1} (given that a doubling of CO_2 would be achieved by year 70 in the CMIP2 simulations). Thus, the results of this study indicate that on an annual basis, the current satellite-based retrieval synthesis and parametric global water cycling estimates can neither provide trend detection nor balanced and/or consistent analyses to verify the range of climate model global hydrologic change projections. Not only must global water cycle observation synthesis continue, so as to reduce the minimum trend that can be detected (e.g., Ziegler et al. 2003), but detection strength may be augmented through trend consistency between global evaporation, precipitation, and precipitable water observations. In this respect, the two order of magnitude discrepancy between annual variations of global $P - E$ and precipitable water must also be reduced. This would include a careful reevaluation of the global ocean evaporation trends. In doing so, the retrieved SSM/I quantities and their trends (on a global and regional scale) as well as their usage in a bulk aerodynamic formula, and whether other inputs to the formula are robust, such as the bulk aerodynamic coefficient (or Dalton number), C_E, must be reexamined. Unfortunately, during the course of this study, an explicit examination of the calculated C_E from the GSSTF algorithm was not possible. Preliminary analysis of the HOAPS-derived C_E shows a very heterogeneous relationship in this regard (i.e., no globally ubiquitous consistency), and likely does not substantially affect the HOAPS trend. The types of diagnoses and reevaluations required to adequately address and improve the

performance of satellite-based ocean turbulent flux estimates (like the GSSTF product) are a key element in the SEAFLUX project (Curry et al. 2004), and there is great promise for improving these global estimates and quantifying uncertainties. Finally, the uncertainty (i.e., consensus) in the estimated global, annual river discharge should be reduced to well below its measured interannual variability, which is on the order of 1–2 × 10^{15} kg yr^{-1}. Until such time, it will be problematic to ascribe unequivocal detection of "significant" global change in observed annual global river discharge.

There is a clear need of a global "vital sign" (e.g., Karl and Trenberth 2003) of the hydrologic system for public awareness and guidance for global policy decisions. However, this study shows that our ability to consistently observe global-scale water cycle components requires a considerable amount of maturing. Such global hydrologic metrics will be valuable to the general public, much like global averaged temperature, in conveying the "status" of global changes in water transport, but credence in such metrics ultimately lay in the quality and consistency of the measurements we use. The ultimate goal of quantifying the degree, causes, and consequences of global hydrologic change will likely be achieved through global hydroclimatological data collection and analysis of event-based precipitation (e.g., Trenberth et al. 2003) and associated hydrologic quantities (e.g., water storage, evaporation, and runoff). In doing so, we will also continue to build upon our regional observational capabilities to detect regional climate change "hot spots" (e.g., Giorgi 2006). Thus, the development of climate-quality-observed global hydrologic data must be sustained and considered a top priority. Such data will ensure the effective analyses, communication, and application of global climate changes (anthropogenic and/or natural) that we observe.

REFERENCES

Adler, R. F., C. Kidd, G. Petty, M. Morissey, and H. M. Goodman, 2001: Intercomparison of global precipitation products: The Third Precipitation Intercomparison Project (PIP-3). *Bull. Amer. Meteor. Soc.,* **82,** 1377–1396.

——, and Coauthors, 2003: The version-2 Global Precipitation Climatology Project (GPCP) monthly precipitation analysis. *J. Hydrometeor.,* **4,** 1147–1167.

Allen, M. R., and W. J. Ingram, 2002: Constraints on future changes in climate and the hydrologic cycle. *Nature,* **419,** 224–232.

Amenu, G. G., and P. Kumar, 2005: NVAP and reanalysis-2 global precipitable water products. *Bull. Amer. Meteor. Soc.,* **86,** 245–256.

Bacmeister, J. T., P. J. Pegion, S. D. Schubert, and M. J. Suarez, 2000: *Atlas of Seasonal Means Simulated by the NSIPP1 Atmospheric GCM.* Vol. 17, NASA Tech. Memo. 2000-104606, 194 pp.

Basist, A., G. D. Bell, and V. Meentemeyer, 1994: Statistical relationships between topography and precipitation patterns. *J. Climate,* **7,** 1305–1315.

Baumgartner, A., and E. Reichel, 1975: *The World Water Balance.* Elsevier, 179 pp.

Bentamy, A., P. Queffeulou, Y. Quilfen, and K. Katsaros, 1999: Ocean surface wind field estimate from satellite active and passive microwave instruments. *IEEE Trans. Geosci. Remote Sens.,* **37,** 2469–2486.

——, K. B. Katsaros, A. M. Mestas-Nuñez, W. M. Drennan, E. B. Forde, and H. Roquet, 2003: Satellite estimates of wind speed and latent heat flux over the global oceans. *J. Climate,* **16,** 637–656.

Berner, E. K., and R. A. Berner, 1987: *The Global Water Cycle: Geochemistry and Environment.* Prentice Hall, 397 pp.

Bosilovich, M., S. D. Schubert, and G. K. Walker, 2005: Global changes of the water cycle intensity. *J. Climate,* **18,** 1591–1608.

Boyer, T. P., S. Levitus, J. I. Antonov, R. A. Licarnini, and H. E. Garcia, 2005: Linear trends in salinity for the World Ocean, 1955-1998. *Geophys. Res. Lett.,* **32,** L01604, doi:10.1029/2004GL021791.

Brunke, M. A., C. W. Fairall, X. Zeng, L. Eymard, and J. Curry, 2003: Which bulk aerodynamic algorithms are least problematic in computing ocean surface turbulent fluxes? *J. Climate,* **16,** 619–635.

Chou, S.-H., R. M. Atlas, C.-L. Shie, and J. Ardizzone, 1995: Estimates of surface humidity and latent heat fluxes over oceans from SSM/I data. *Mon. Wea. Rev.,* **123,** 2405–2424.

——, W. Chao, and M.-D. Chou, 2000: Surface heat budgets and sea surface temperature in the Pacific warm pool during TOGA COARE. *J. Climate,* **13,** 634–649.

——, E. Nelkin, J. Ardizzone, R. M. Atlas, and C.-L. Shie, 2003: Surface turbulent heat and momentum fluxes over global oceans based on the Goddard satellite retrievals, version 2 (GSSTF2). *J. Climate,* **16,** 3256–3273.

Colton, M. C., and G. A. Poe, 1999: Intersensor calibration of DMSP SSM/Is: F-8 to F-14, 1987-1997. *IEEE Trans. Geosci. Remote Sens.,* **37,** 418–439.

Conkright, M. E., and Coauthors, 2002: *Introduction.* Vol. 1, *World Ocean Database 2001,* NOAA Atlas NESDIS 42, 167 pp.

Curry, J. A., and Coauthors, 2004: SEAFLUX. *Bull. Amer. Meteor. Soc.,* **85,** 409–424.

Curry, R., B. Dickson, and I. Yashayaev, 2003: A change in the freshwater balance of the Atlantic Ocean over the past four decades. *Nature,* **426,** 826–829.

Curtis, S., R. Adler, G. Huffman, E. Nelkin, and D. Bolvin, 2001: Evolution of tropical and extratropical precipitation anomalies during the 1997-1999 ENSO cycle. *Int. J. Climatol.,* **21,** 961–971.

Dai, A., and K. Trenberth, 2002: Estimates of freshwater discharge from continents: Latitudinal and seasonal variations. *J. Hydrometeor.,* **3,** 660–687.

Diak, G. R., J. R. Mecikalski, M. C. Anderson, J. M. Norman, W. P. Kustas, R. D. Torn, and R. L. DeWolf, 2004: Estimating land surface energy budgets from space. *Bull. Amer. Meteor. Soc.,* **85,** 65–78.

Diaz, H. F., M. P. Hoerling, and J. K. Eishceid, 2001: ENSO variability, teleconnections, and climate change. *Int. J. Climatol.,* **21,** 1845–1862.

Dirmeyer, P. A., and L. Tan, 2001: A multi-decadal global land-surface data set of state variables and fluxes. COLA Tech. Rep. 102, Center for Ocean–Land–Atmosphere Studies, Calverton, MD, 43 pp.

——, X. Gao, and T. Oki, 2002: The Second Global Soil Wetness Project (GSWP2). *GEWEX News,* No. 37, International GEWEX Project Office, Silver Spring, MD, 75 pp.

——, Z. Guo, and X. Gao, 2004: Comparison, validation, and transferability of eight multiyear global soil wetness products. *J. Hydrometeor.,* **5,** 1011–1033.

Fairall, C. W., E. F. Bradley, D. P. Rogers, J. B. Edson, and G. S. Young, 1996: Bulk parameterization of air-sea fluxes for Tropical Ocean Global Atmosphere Coupled Ocean–Atmosphere Response Experiment. *J. Geophys. Res.,* **101,** 3747–3764.

Fekete, B. M., C. J. Vörösmarty, and W. Grabs, 1999: Global, composite runoff fields based on observed river discharge and simulated water balances. GRDC Rep. 22, Global Runoff Data Center, Koblenz, Germany, 36 pp.

——, ——, and ——, 2002: High resolution fields of global runoff combining observed river discharge and simulated water balances. *Global Biogeochem. Cycles,* **16,** 1042, doi:10.1029/1999GB001254.

——, ——, J. O. Roads, and C. J. Willmott, 2004: Uncertainties in precipitation and their impacts on runoff estimates. *J. Climate,* **17,** 294–304.

Giorgi, F., 2006: Climate change hot-spots. *Geophys. Res. Lett.,* **33,** L08707, doi:10.1029/2006GL025734.

Groisman, P. Ya., R. W. Knight, T. R. Karl, D. R. Easterling, B. Sun, and J. H. Lawrimore, 2004: Contemporary changes of the hydrological cycle over the contiguous United States:

Trends derived from in situ observations. *J. Hydrometeor.,* **5,** 64–85.

——, ——, D. R. Easterling, T. R. Karl, G. C. Hegerl, and V. N. Razuvaev, 2005: Trends in intense precipitation in the climate record. *J. Climate,* **18,** 1326–1350.

Hollingsworth, A., and C. Pfrang, 2005: A preliminary survey of ERA-40 users developing applications of relevance to GEO (Group on Earth Observations). *ECMWF Newsletter,* No. 104, ECMWF, Reading, United Kingdom, 5–9.

Hornberger, G. M., and Coauthors, 2001: A plan for a new science initiative on the global water cycle. U.S. Global Change Research Program, Washington, DC, 118 pp.

Houser, P. R., and J. K. Entin, 2005: NASA Energy and Water Cycle Study (NEWS). *GEWEX News,* No. 15, International GEWEX Project Office, Silver Spring, MD, 5–6.

Huffman, G. J., 1997: Estimates of root-mean square random error for finite samples of estimated precipitation. *J. Appl. Meteor.,* **36,** 1191–1201.

Jaeger, L., 1976: *Monatskarten des Niederschlags für die ganze Erde.* Vol. 18 (139), Berichte des Deutschen Wetterdienstes, 38 pp.

Janowiak, J., A. Gruber, C. R. Kondragunta, R. E. Livezy, and G. J. Huffman, 1998: A comparison of the NCEP–NCAR reanalysis precipitation and the GPCP rain gauge–satellite combined dataset with observational error considerations. *J. Climate,* **11,** 2960–2979.

Karl, T. R., and K. E. Trenberth, 2003: Modern global climate change. *Science,* **302,** 1719–1723.

Kayane, I., 1986: Water of the world. *World-Wide Weather,* K. Takahashi, Ed., A. A. Balkema, 25–31.

Kidd, C., 2001: Satellite rainfall climatology: A review. *Int. J. Climatol.,* **21,** 1041–1066.

Kiktev, D., D. M. H. Sexton, L. Alexander, and C. K. Folland, 2003: Comparison and modeled and observed trends in indices of daily climate extremes. *J. Climate,* **16,** 3560–3571.

Kinter, J. K., and Y. Shukla, 1990: The global hydrologic and energy cycles: Suggestions for studies in the pre-Global Energy and Water Cycle Experiment (GEWEX). *Bull. Amer. Meteor. Soc.,* **71,** 181–189.

Koblinsky, C. J., P. Hildebrand, D. LeVine, F. Pellerano, Y. Chao, W. Wilson, S. Yueh, and G. Lagerloef, 2003: Sea surface salinity from space: Science goals and measurement approach. *Radio Sci.,* **38,** 8064, doi:10.1029/2001RS002584.

Korzun, V. I., 1978: *World Water Balance and Water Resources of the Earth* (English translation). UNESCO Press, 663 pp.

Kubota, M., A. Kano, H. Muramatsu, and H. Tomita, 2003: Intercomparison of various surface latent heat flux fields. *J. Climate,* **16,** 670–678.

Leese, J. A., 2001: Coordinated Enhanced Observation Period (CEOP) implementation plan. *GEWEX News,* No. 36, International GEWEX Project Office, Silver Spring, MD, 113 pp.

Lettenmaier, D. P., E. F. Wood, and J. R. Wallis, 1994: Hydroclimatological trends in the continental United States, 1948–1988. *J. Climate,* **7,** 586–607.

Mehta, V. M., A. J. DeCandis, and A. V. Mehta, 2005: Remote-sensing-based estimates of the fundamental global water cycle: Annual cycle. *J. Geophys. Res.,* **110,** D22103, doi:10.1029/2004JD005672.

Meissner, T., D. Smith, and F. Wentz, 2001: A 10 year intercomparison between collocated Special Sensor Microwave Imager ocean surface wind speed retrievals and global analyses. *J. Geophys. Res.,* **106,** 11 731–11 742.

Milly, P. C. D., R. T. Wetherald, K. A. Dunne, and T. L. Del-

worth, 2002: Increasing risk of great floods in a changing climate. *Nature,* **415,** 514–517.

Mischwaner, K., and A. E. Dessler, 2004: Water vapor feedback in the tropical upper troposphere: Model results and observations. *J. Climate,* **17,** 1272–1282.

National Research Council, 1986: *Global Change in the Geosphere–Biosphere.* National Academies Press, 91 pp.

New, M., M. Todd, M. Hulme, and P. Jones, 2001: Precipitation measurements and trends in the twentieth century. *Int. J. Climatol.,* **21,** 1899–1922.

Nijssen, B., G. M. O'Donnell, D. P. Lettenmaier, D. Lohmann, and E. F. Wood, 2001: Predicting the discharge of global rivers. *J. Climate,* **14,** 3307–3323.

Oki, T., T. Nishimura, and P. Dirmeyer, 1999: Assessment of annual runoff from land surface models using Total Runoff Integrating Pathways (TRIP). *J. Meteor. Soc. Japan,* **77,** 235–255.

Peixoto, J. P., and M. A. Kettani, 1973: The control of the water cycle. *Sci. Amer.,* **228,** 46–61.

——, and A. H. Oort, 1992: *Physics of Climate.* American Institute of Physics, 520 pp.

Räisänen, J., 2002: CO_2-induced changes in interannual temperature and precipitation variability in 19 CMIP2 experiments. *J. Climate,* **15,** 2395–2411.

Randel, D. L., T. H. Vonder Haar, M. A. Ringerud, G. L. Stephens, T. J. Greenwald, and C. L. Combs, 1996: A new global water vapor dataset. *Bull. Amer. Meteor. Soc.,* **77,** 1233–1246.

Reynolds, R. W., and T. M. Smith, 1994: Improved global sea surface temperature analyses using optimum interpolation. *J. Climate,* **7,** 929–948.

Roads, J. O., S.-C. Chen, M. Kanamitsu, and H. Juang, 1999: Surface water characteristics in the NCEP Global Spectral Model and Reanalysis. *J. Geophys. Res.,* **104,** 19 307–19 327.

Rodell, M., and Coauthors, 2004: The global land data assimilation system. *Bull. Amer. Meteor. Soc.,* **85,** 381–394.

Roy, S. R., and R. C. Balling Jr., 2004: Trends in extreme daily precipitation indices in India. *Int. J. Climatol.,* **24,** 457–466.

Schlosser, C. A., and B. Kirtman, 2005: Predictable skill and its association to sea-surface temperature variations in an ensemble climate simulation. *J. Geophys. Res.,* **110,** D19107, doi:10.1029/2005JD005835.

Seager, R., R. Murtugudde, A. Clement, and C. Herweijer, 2003: Why is there an evaporation minimum at the equator? *J. Climate,* **16,** 3793–3802.

Shiklomanov, I. A., 1998: World water resources: A new appraisal and assessment for the 21st century. UNESCO, 40 pp.

Soden, B. J., 2000: The sensitivity of the tropical hydrological cycle to ENSO. *J. Climate,* **13,** 538–549.

——, R. T. Wetherald, G. L. Stenchikov, and A. Robock, 2002: Global cooling following the eruption of Mt. Pinatubo: A test of climate feedback by water vapor. *Science,* **296,** 727–730.

Soluri, E. A., and V. A. Woodson, 1990: World vector shoreline. *Int. Hydrogr. Rev.,* **68,** 27–36.

Speidel, D. H., and A. F. Agnew, 1982: *The Natural Geochemistry of our Environment.* Westview Press, 214 pp.

Trenberth, K. E., and C. J. Guillemot, 1998: Evaluation of the atmospheric moisture and hydrologic cycle in the NCEP/NCAR reanalyses. *Climate Dyn.,* **14,** 213–231.

——, A. Dai, R. M. Rasmussen, and D. B. Parons, 2003: The changing character of precipitation. *Bull. Amer. Meteor. Soc.,* **84,** 1205–1217.

——, J. Fasullo, and L. Smith, 2005: Trends and variability in column-integrated atmospheric water vapor. *Climate Dyn.,* **24,** 741–758.

Verschuren, D., K. R. Laird, and B. F. Cumming, 2000: Rainfall and drought in equatorial east Africa during the past 1,100 years. *Nature,* **403,** 410–414.

Vonder Harr, T., and Coauthors, 2003: Continuation of the NVAP global water vapor data sets for Pathfinder science analysis Science and Technology Corp. STC Tech. Rep. 3333, 44 pp. [Available online at http://eosweb.larc.nasa.gov/PRODOCS/nvap/sci_tech_report_3333.pdf.]

Wentz, F. J., and M. Schabel, 2000: Precise climate monitoring using complementary satellite data sets. *Nature,* **403,** 414–416.

Xie, P., and P. A. Arkin, 1997: Global precipitation: A 17-year monthly analysis based on gauge observations, satellite estimates, and numerical model outputs. *Bull. Amer. Meteor. Soc.,* **78,** 2539–2558.

Yang, F., A. Kumar, M. E. Schlesinger, and W. Wang, 2003: Intensity of hydrological cycles in warmer climates. *J. Climate,* **16,** 2419–2423.

Yin, Y., A. Gruber, and P. Arkin, 2004: Comparison of the GPCP and CMAP merged gauge–satellite monthly precipitation products for the period 1979–2001. *J. Hydrometeor.,* **5,** 1207–1222.

Ziegler, A. D., J. Sheffield, E. P. Maurer, B. Nijssen, E. F. Wood, and D. P. Lettenmaier, 2003: Detection of intensification in global- and continental-scale hydrological cycles: Temporal scale of evaluation. *J. Climate,* **16,** 535–547.